Utrecht University

Master Thesis

Nanomaterials Science

In situ Micro-Spectroscopic Investigation on the Stability of TCNQ-loaded HKUST-1 Single Crystals in H_2O Environment

Author:
E. C. van der Feltz, BSc

Supervisor:
Dr. ir. M. Filez
Examiner:
Prof. dr. ir. B. Weckhuysen

Utrecht University

June, 2018

Metal Organic Frameworks (MOF) are a class of porous, crystalline materials with a wide variety of applications ranging from gas sensing to catalysis and drug delivery. More particularly, MOFs have appeared to be excellent candidates for the incubation of guest species. An example of this is the Cu-BTC MOF named HKUST-1, which can be readily loaded by TCNQ, a redox-active compound, which significantly enhances electric conductivity. It is known that H_2O can have a detrimental effect on HKUST-1, often binding to coordinatively unsaturated Cu centres which can trigger metal linker defect formation and even subsequent structural collapse. Considering TCNQ's location within the MOF structure, H_2O could have an adverse effect on the stability of TCNQ. The influence of H_2O on the stability of TCNQ needs to be understood in order to further improve upon electric conductivity. In this work, the hydration of TCNQ-loaded HKUST-1 single crystals is monitored and their diffusion properties assessed by means of vibrational micro-spectroscopic techniques. The intracrystal distribution of TCNQ is investigated by Raman microscopy and regions of enhanced concentration were observed at the crystal edges. Subsequent *in situ* hydration experiments probed by IR microscopy suggest decreased diffusion of H_2O at the crystal edge resulting in the accumulation of H_2O. Post-hydration analysis of the TCNQ distribution point out that the TCNQ enriched edge regions became equally distributed. This is interpreted as the possible result of the hydrolysis of TCNQ's nitrile bond. The potential applications of electric conductivity in MOFs are profound, yet hydrothermal stability is required. Therefore understanding of the influence of H_2O on the guest species and the structure is paramount. Most diffusion experiments of H_2O in HKUST-1 has been performed on the bulk scale, yet the effect of H_2O on the single crystal level remains unexplored. Careful examination of single crystals during diffusion experiments could shed light on fundamental information such as the interaction of H_2O with TCNQ and the MOF architecture. Along with bulk diffusion finds, these fundamental insights could eventually culminate into rational design of novel materials with highly tunable electric conductivity.

Contents

List of Figures

Chapter 1

Introduction

1.1 Metal Organic Frameworks

Metal Organic Frameworks (MOFs) are a class of highly porous materials with a wide variety of applications such as gas storage/separation, chemical sensors, drug delivery and catalysis.[1–4] In addition to these applications, MOFs have also earned academic attention as their architecture is easily tunable. This enables materials with properties tailored to their respective application.

1.1.1 Structure and properties

All MOFs are, as the name infers, 2-dimensional (thin-films) or 3-dimensional (single crystals) frameworks comprised of metal nodes interconnected by organic linkers.[5] These materials are highly porous with large internal surface areas. The primary building blocks for these materials are metaloxide centres and organic linkers. As there is a wide variety of metaloxides and organic linkers, many different MOFs are possible. Dependent on the coordination number of the metal centres and the denticity[i] of the linkers, secondary building blocks (SBUs) are formed which in turn culminate into the complete framework.[6] This is schematically depicted in Figure 1.1.

Most properties can be derived directly from the centres and linkers in question. This is often exploited in MOF-based chemical sensors. Selectivity towards specific chemical interactions such as H-bonding and $\pi - \pi$ interactions differ per MOF rendering certain materials more suitable than others.[2] Besides certain interactions, size restraints also contribute to the overall selectivity of a MOF. As MOFs allow for very easy tuning of the pore volume and windows, they are an excellent class of material when selecting chemicals based on size. However, for many applications, one requires selectivity towards many properties of certain adsorbates. Literature provides comprehensive guides for the myriad of MOFs and their corresponding applications.[7]

Besides inherent properties due to metal centres and organic linkers, it is also possible to tune properties of a MOF by impregnating them with guest species. An example of this is the impregnation of the MOF HKUST-1 with the molecule TCNQ[ii] to obtain electrical conductivity.[8] The implications of this procedure on the properties of HKUST-1 will be discussed elaborately in this study.

[i] In coordination chemistry, each linker has a certain amount of groups that will bind to the metal centre. The number of groups for each linker (monodentate, bidentate, tridentate etc.) is referred to as the denticity.

[ii] Both HKUST-1 and TCNQ will be addressed in the coming section.

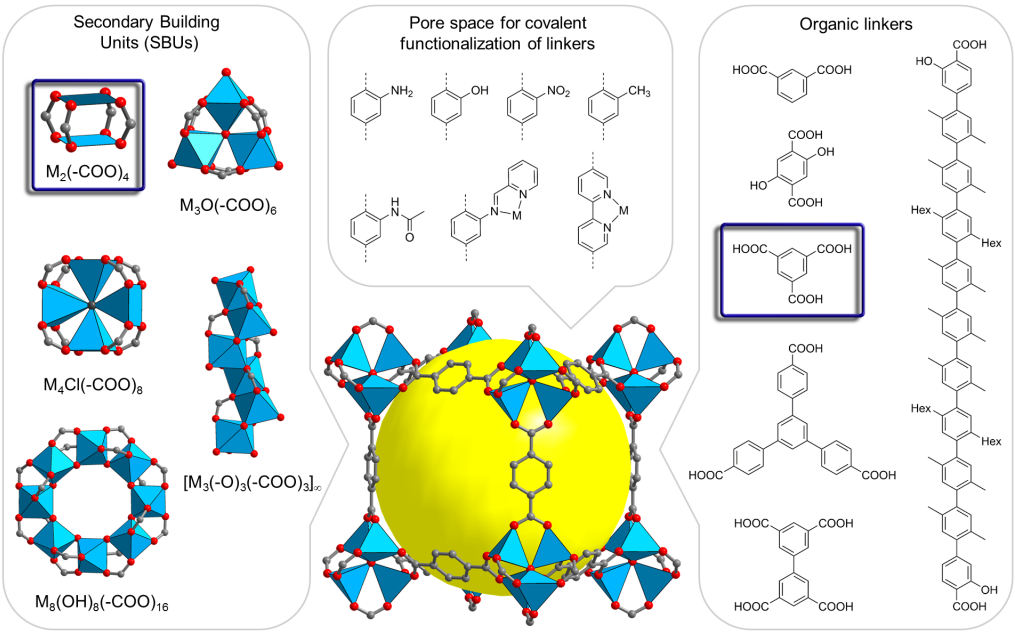

Figure 1.1: This depicts the building blocks of a typical MOF. Primary building blocks are not depicted. The blue polyhedra represent metal atoms and the red dots represent oxygen atoms. The grey organic linkers connect the metal nodes which in turn shape the empty pore space (depicted as the yellow sphere). HKUST-1's metal node and organic linker are highlighted. Reproduced from The Florida Institute of Technology.[9]

1.1.2 HKUST-1

HKUST-1 (*H*ong *K*ong *U*niversity of *S*cience and *T*echnology - 1) or Cu-BTC (Copper *B*enzene *T*ricarboxylic *A*cid) is a copper-based MOF with tridentate linkers. The first report of the synthesis of HKUST-1 was reported in 1999 by Chui et al.[10] The metal centres are comprised of two Cu^{2+} ions connected via four linkers forming a pseudooctahedral coordination sphere. This system resembles a paddle wheel structure with four linkers as paddles. This structure is visually depicted in Figure 1.2. Additionally, a solvent group can bind axially at each copper atom along the Cu-Cu axis. This axially bound group could be exchanged for numerous types of guest species. These groups could have profound implications on the properties of this MOF.[11]

The effect of H_2O on HKUST-1 The interactions between HKUST-1 and water are subject for research for many scientists. For some applications these interactions could be considered benign, as the structure is reported to be able to take up roughly 40 wt.% of water.[12] This is possible due to their large surface area ($\approx$ 2000 m^2/g) and large pore volume ($\approx$ 1 cm^3/g).[13] This merits their use as vapour sensors.

However, there are other interactions which are ambiguously either benign or malign. In the case of completely activated HKUST-1, where all axially bound solvent molecules have been removed, an unsaturated metal centre is 'exposed'. This state can be recognized by the dark navy blue colour of the crystals. When H_2O enters the MOF structure, it could bind axially causing the paddle wheel structure to expand along the Cu-Cu axis. The distance increase is also accompanied by a decrease in energy of 69.4 kJ/mol Cu as the H_2O group binds[11]. In addition to the energy change, the colour shifts from dark navy blue to a light cyan blue as the coordination number of the Cu changes as well as the distortion of the octahedral cage.[14] If there is no excess H_2O, other than the coordinatively bound groups, beneficial effects can emerge such as an improved gas

uptake towards CO_2. This is caused by the increase of Coulombic energy in the structure due to the presence of H_2O. Given the electrostatic interactions[iii] between H_2O and CO_2, the presence of H_2O is beneficial for the adsorption of CO_2.[13] This effect is useful for the gas capture and separation of CO_2, yet only if the quantity of H_2O is small ($\approx$ 4 wt.%).

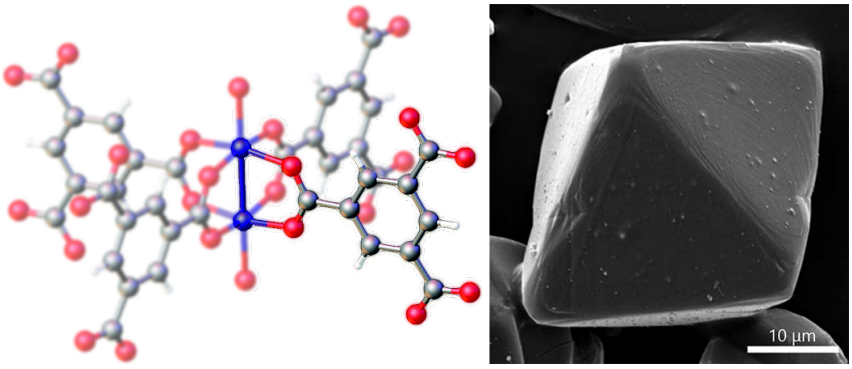

Figure 1.2: Left: In this graphical representation of HKUST-1, the paddlewheel structure can be seen clearly. One of the paddles is highlighted and each carboxylic group will bind to another paddlewheel Cu-centre. Colour coding is as follows: Blue = Copper, Red = Oxygen, Grey = Carbon, White = Hydrogen. Right: SEM Micrograph of an HKUST-1 crystal. Modified from Worrall et al. and Wee et al.[16, 17]

In case of larger quantities, the pore structure will occlude, and gas uptake is reduced. Moreover, in the case of prolonged exposure to an excess of H_2O, it is reported that the structure will degrade due to metal-linker defects. This process is depicted in Figure 1.3. Todaro et al. reported on the decomposition of the structure due to the presence of an excess of H_2O.[18] After prolonged exposure to H_2O the Cu-O bond will be irreversibly hydrolysed causing metal-linker defects. These defects cause pore occlusion and structure degradation. This has also been explored by Majano et al. where HKUST-1 is controllably degraded by various ways of inducing H_2O.[19] They have reported on the gradual hydrolysis on metal linker-bonds and the subsequent degradation of the structure. As the structure degrades, the uptake of guest species diminishes, as been reported by Heinke et al.[20] Instead of CO_2 , cyclohexane was the guest molecule of choice, but it is expected to show similar behaviour to CO_2 as for its large non-zero quadropole moment.[21]

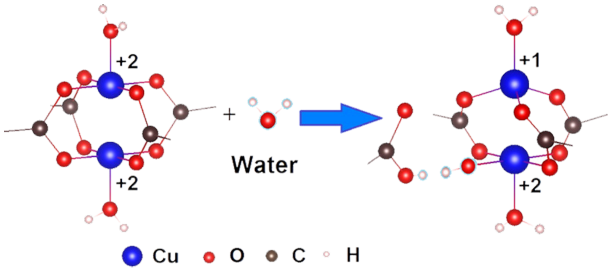

(a) The proposed mechanism as to how H_2O causes metal-linker defects in the HKUST-1 structure. As H_2O hydrolyses the Cu-O bond, it separates the linker from the metal centre and the Cu-ion is reduced. Modified from Todaro et al.[18]

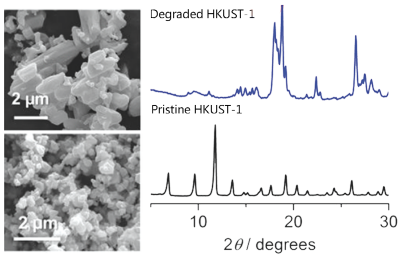

(b) Prolonged exposure to H_2O causes the overal structure to decompose. This can be seen by XRD after exposing HKUST-1 to 77% humidity for 2.5 months. Modified from Majano et al.[19]

Figure 1.3: Degradation of HKUST-1 by H_2O.

[iii]The quadrupole moment of CO_2 will interact with the electric field gradient of H_2O. As the amount of coordinatively bound H_2O is increased, the electric field gradient will increase along with it. This explanation has been tested by using N_2 as guest species. As expected, no uptake was found as for the very small quadrupole moment of N_2.[15]

1.2 TCNQ

TCNQ, tetracyanoquinodimethane, is a conjugated redox-active organic compound, which is often used for its charge transferring properties. The structure is displayed in Figure 1.4. As it readily forms compounds with metals, it is a popular compound to use as a dopant in order to improve electrical conductivity of otherwise insulating materials.[22] This also is the case for HKUST-1, which is normally a semi-conductor with a band gap of 2.5-3.5 eV. By loading the MOF with TCNQ, the band gap reduces to 1.4 eV.[23, 24] This yields a MOF-TCNQ compound of which the electrical conductivity has increased by several orders of magnitude.

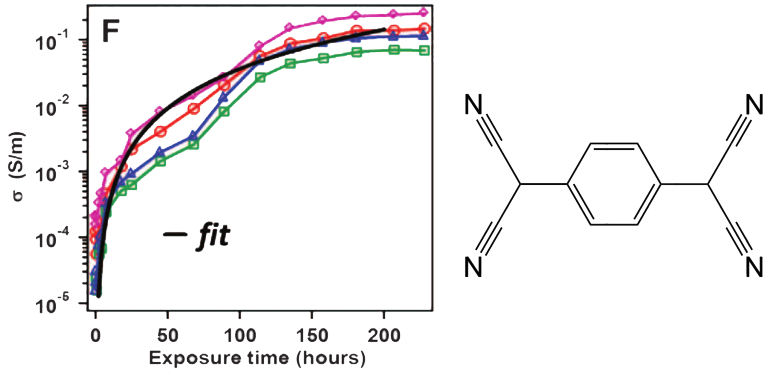

Figure 1.4: Left: The electrical conductivity increases with several orders of magnitude as HKUST-1 is exposed to TCNQ for prolonged periods. This was measured for four samples and they all show a similar trend. The black line is a fit over the data. Right: The conjugated compound TCNQ, tetracyanoquinodimethane. Modified from Talin et al.[8]

As mentioned earlier, the colour of HKUST-1 in its activated form (i.e. no axially bound solvent molecules) is a dark navy blue. Whereas it changes to a lighter cyan blue upon adsorption of solvent. This is due to the fact that the dimensions of the octahedral cage of the Cu-ions change upon adsorption-desorption which gives prominence to the d-d transitions of Cu^{2+} species. In perfect octahedral symmetries d-d transitions are dipole forbidden, yet the presence of solvent molecules induces Jahn-Teller distortions[iv], resulting in intenser d-d bands. Prestipino et al. performed UV-Vis spectroscopy measurements and reported on the appearance of a high-energy shoulder at 18400 cm^{-1} in the d-d band centred at 11900 cm^{-1} as the structure becomes activated.[25] The associated absorption of visible light (18400 cm^{-1} = 543 nm) reduces the amount of scattered green light, rendering the overall colour as darker and deeper blue.

This is a rather convenient characteristic of HKUST-1 as it allows for easy visual examination on whether the structure is activated or not. However, Talin et al. pointed out that when TCNQ is incorporated in the structure, the colour shift from dark navy blue to cyan does not occur upon exposure to moist atmosphere.[8] Considering the proposed position of TCNQ in the pores of HKUST-1 (see Figure 1.5) one could assume that TCNQ is not displaced by H_2O and hinders H_2O from entering the pores. Whether this is the case merits further research.

[iv] The Jahn-Teller effect entails the breaking of geometric symmetry due to changing electronic configurations. This causes a loss in degenerate electronic states.

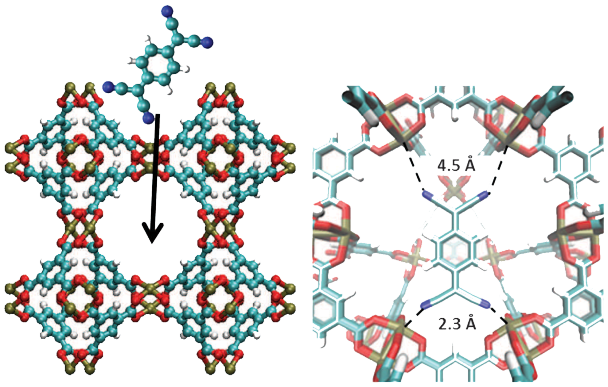

Figure 1.5: TCNQ in a pore of HKUST-1. The molecule spans itself accross the pore binding each nitrile group to a copper cluster. This both greatly enhances the electrical conductivity of the structure and it is assumed that it occludes the pores for water entry. Modified from Talin et al.[8]

1.3 Approach

In order to probe the effect of H_2O on pristine HKUST-1 and TCNQ-infused HKUST-1, micro-spectroscopic techniques (specifically IR microscopy and Raman microscopy) will be employed. As opposed to extensive research reporting on bulk degradation and diffusion of MOFs[25–29], a single crystal study is presented in this work. By combining micro-spectroscopic techniques, chemical insight with spatial resolution can be revealed. The bulk of the research will be based on Raman microscopy and infrared microscopy, whereas electron microscopy and x-ray diffraction will serve as supporting techniques. A detailed description will follow in due course.

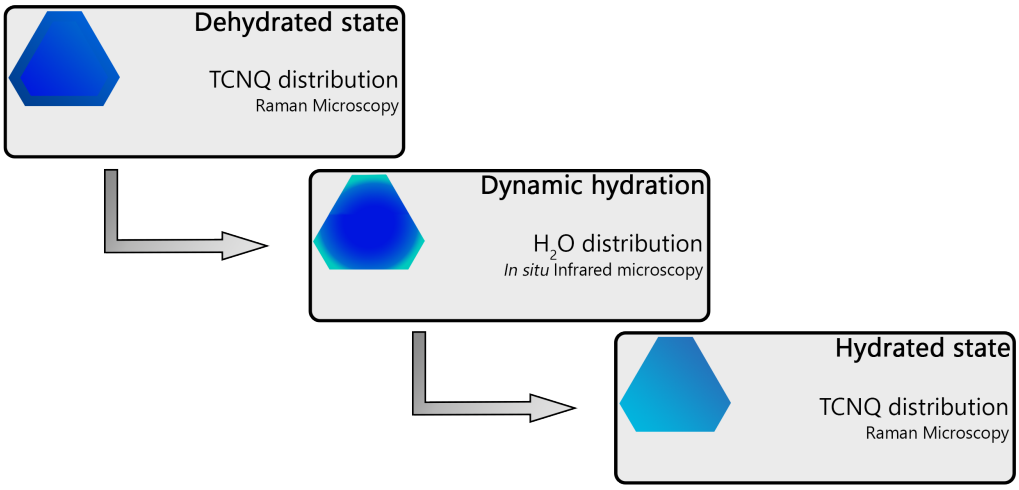

Figure 1.6: This diagram represents the approach of the research. Raman microscopy will provide insight into the role of TCNQ and infrared microscopy for the the role of H_2O .

In Figure 1.6 the outline of the approach of the research is presented. To elucidate the stability of TCNQ against H_2O vapour, two samples were compared: unaltered activated HKUST-1 (hereafter referred to as pristine HKUST-1) and TCNQ-infused HKUST-1. Considering the limited spatial resolution of infrared microscopy, both samples were synthesized as large crystals. Before the actual hydration experiment (i.e. the dehydrated state), Raman microscopy will be used to investigate the distribution of TCNQ and to determine suitable candidates for *in situ* IR microscopy

hydration experiments. Afterwards, both pristine and TCNQ-infused HKUST-1 will be gradually hydrated during *in situ* infrared microscopy imaging. *In situ* X-ray diffraction will serve as a tool to determine the stability of the samples under various temperatures and atmospheres. Data analysis should provide spatially and temporally resolved information regarding the hydration of both samples. Subsequently, the TCNQ-infused HKUST-1 sample will be imaged once more by means of Raman microscopy to probe TCNQ's reaction to H_2O. Finally, the Raman microscopy images will be corroborated by scanning electron microscopy in order to account for possible anomalies.

Chapter 2

Methods and Materials

In this chapter all experimental methods and associated materials are described. The underlying principles will be described for all utilized characterization techniques and the applied analytical methods will be addressed.

2.1 Methods

All characterization techniques and analytical methods will be described in this section. As *in situ* techniques three methods were utilized: X-ray diffraction, Raman microscopy and infrared microscopy in order to probe the sensitivity of the materials with respect to water vapour. Scanning electron microscopy and Raman microscopy were used as *ex situ* techniques to obtain insight into the general morphology of the samples and distribution of chemical species.

2.1.1 *In situ* X-Ray Diffraction (XRD)

Diffraction of light (or that of any wave) occurs when the light wave encounters an object with comparable dimensions to its wavelength. The wave will bend around the object and diffract to a certain degree which depends on the relative dimensions of the object and wave. If the wave is to encounter many objects, the resulting diffracted waves will interfere with each other destructively or constructively, dependent on the orientation of the objects.[30] In case of periodically spaced objects, constructive interference occurs at specific angles, resulting in a diffraction pattern. The angles at which constructive interference is to occur, depends on the spacing of the point scatterers (the periodically spaced objects) and the wavelength of the light. This is mathematically described by Bragg's Law in Equation (2.1),

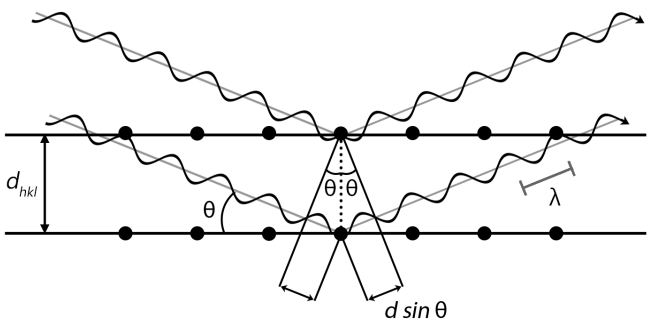

Figure 2.1: Schematic representation of the requirements for Bragg scattering. According to Bragg's Law, constructive interference only occurs when $n\lambda = 2d\sin\theta$.

$$n\lambda = 2d\sin\theta \tag{2.1}$$

in which λ equals the wavelength, d the spacing of the objects and θ the diffraction angle. This relation is visualized in Figure 2.1.

This scheme represents the condition for Bragg scattering. If two coherent light waves propagate towards two point scatterers, they will be scattered in a specular fashion. However, as Figure 2.1 shows, a phase shift could occur as the light paths are not of identical length. The difference in the length of the light path is twice that of $d\sin\theta$. If there is a phase shift, the waves will interfere destructively, but if there is no phase shift, the waves will constructively interfere. The presence of this phase shift depends on the angle θ and wavelength. If the angle of incidence and wavelength are such that the difference in the length of the light path ($2d\sin\theta$) is equal to an integer times the wavelength ($n\lambda$), constructive interference will occur, as described by Equation (2.1).[31]

Diffraction gratings or slits work according to this theoretical framework. Yet this is also applicable to atoms, which can also be considered as point scatterers. When the electric field component of a light wave encounters an atom's electron cloud, the cloud becomes polarized rendering the cloud a dipole. As the incident electric field oscillates, the dipole will also oscillate at the same frequency producing radiation of the same frequency as the incident light. This is called Rayleigh scattering or elastic scattering, where no energy is lost.[32]

If the atoms are periodically spaced, as is the case for crystals, Bragg scattering could occur if the atom spacing is comparable with the incident wavelength. This merits the use of X-rays. With a very well defined wavelength and by varying the angle 2θ[i], one is able to deduce the lattice parameter d of a crystalline sample. This parameter provides information on the size and shape of the crystal unit cell. It is a vector quantity related to a crystallographic plane within a unit cell. Each plane has its corresponding parameter d as it is the vector from the origin of the unit cell perpendicular to the plane. Crystallographic planes are identified by means of Miller indices[ii], therefore the lattice parameter d is also labelled with the corresponding Miller indices. The lattice parameter d, with its corresponding crystallographic plane is visualized in Figure 2.2. If Bragg scattering is to occur at a certain angle 2θ, one could calculate the parameter d which is an indication of the existence of a certain crystallographic plane.[33]

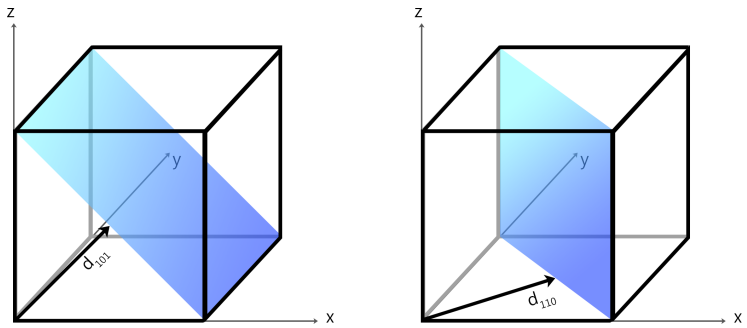

Figure 2.2: In this cubic cell, the crystallographic planes (101) and (110) are depicted. This indicates that the left hand plane intersects the x- and z axes at the vertex of the cube whereas it never intersects the y axis (i.e. it is parallel). The right hand plane intersects axes x and y at the vertex of the cube and is parallel to the z axis. The lattice parameter d extends from the origin of the unit cell to the plane at a 90° angle.

[i] As the angle of incidence θ and the angle of diffraction θ must be identical for Bragg scattering, it is common practice to refer to scattering angles as angle 2θ instead of angle θ. This is clearly visualized in Figure 2.3.

[ii] Miller indices define a plane within the unit cell by describing the intersects of the plane with the edges of the cell. Each index is the reciprocal of the location of the intersect.

For a typical XRD experiment, the X-ray source and detector are mounted on a semicircle around the stationary sample. By adjusting the position of both source and detector, one varies the angle θ as can be seen from Figure 2.3. The focussing distance of the source and detector are fixed by the radius of the semicircle. This geometry is commonly referred to as Bragg-Brentano geometry. The X-rays are generated by bombarding a specific filament (often Cu, Co, Mo or W) with electrons to generate X-rays which leave the tube through an X-ray transparent window. Specified optics and slits are used for focusing and filtering β- and L-radiation in order to obtain monochromatic and parallel X-rays.

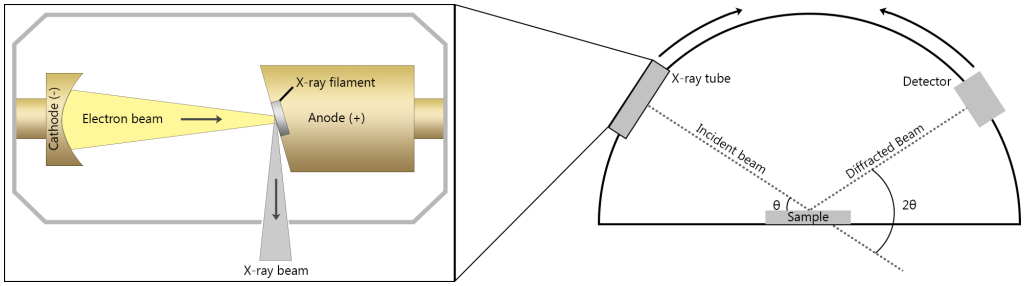

Figure 2.3: This simplified scheme visualizes the working principle of an X-ray diffractometer. The X-ray tube on the left generates the X-ray beam. By moving the X-ray tube and detector with respect to the stationary sample, one is able to vary the angle θ.

Experimental section All experiments were performed on a Bruker AXS D8 Advance 120 machine, Co-K_α radiation ($\lambda = 1.79$ Å) using divergence slits in Bragg-Brentano geometry. Various temperature and atmospheric programs were utilized in order to probe the sensitivity of the samples. These will be discussed in more detail in Chapter 4. All data analysis was performed using Diffrac.Eva V4.2 software by Bruker AXS.

2.1.2 Scanning Electron Microscopy

Scanning electron microscopy (SEM) is very similar to optical microscopy. In both types of microscopy, one directs radiation towards a sample, which interacts with the sample and after passing through various optics is detected. The main difference is the type of radiation. In optical microscopy, one probes the sample with electromagnetic radiation (often visible light) which reflects of the sample and forms the image on the detector. However, for electron microscopy the probe consists of particle radiation (electrons) at relativistic speeds which has the benefit of much shorter wavelengths. Due to the Rayleigh criterion[iii], the maximum resolution one can achieve is limited by the wavelength of the radiation. In the case of optical microscopy, which uses visible light ≈ 400 nm - 700 nm, the maximum resolution is roughly half that of the wavelength. But when using electrons with an energy of 12 keV, the de Broglie wavelength[iv] is equal to 0.01 nm with a theoretical resolution of ≈ 0.005 nm. Many aspects such as optics and electronic interactions increase this theoretical resolution limit, yet it greatly surpasses optical microscopy.[34, 35]

[iii] The Rayleigh criterion limits the resolvable information from a wave. As a wave passes through a slit or lens of comparable dimensions to the wavelength of the wave, the wave will diffract. The diffraction angle increases as the wavelength approaches the width of the slit. As soon as the wavelength and the slit are of the same size, the diffraction angle will be 90° spreading the wave completely until the diffraction plane. This renders the information of the source of the wave unresolvable.

[iv] All matter can behave like a wave and therefore has its corresponding wavelength. This de Broglie wavelength is defined as $\lambda = h/p$. As an electron travelling at ≈ 20% light speed has a much greater momentum than a photon, its wavelength is much shorter than that of a photon. At even higher speeds (operating voltages of the microscope) relativistic effects such as time dilation, length contraction and mass increase shorten the wavelength even further.

The electrons can interact with the sample in various ways as depicted in Figure 2.4. They either interact elastically (indicated by blue arrows), where there is no energy exchange between the incident electron and the sample, or inelastically (indicated by black arrows), which is accompanied by an energy exchange. Elastic electron interactions are analogous to Rayleigh scattering and the direction of the scattered electron can be either along the path of incidence or against it. When an incident electron travels in the vicinity of an atom, it encounters a Coulombic force from the atom's positively charged nucleus which bends the path of the direction. If the distance between the incident path and an encountered atom's nucleus is large, the scattering angle is small as the Coulombic force is small. But given the fact that the Coulombic force is inversely related to the squared distance (as can be seen from Equation (2.2)), a large scattering angle is observed for electrons travelling closely by the nucleus. This scattering angle could become larger than 90° resulting in a back-scattered electron (BSE) which (partially) constitutes the image obtained using SEM. Besides the distance, the charge of the nucleus also contributes to the exerted force. Therefore heavier elements (large Z-value) generate more BSE's improving their visibility on the SEM image. If the electrons are scattered but remain directed along the path of incidence they could be used for Transmission Electron Microscopy. There are many more types of elastic interactions but these are beyond the scope of this review, therefore only the above-mentioned interactions are discussed.

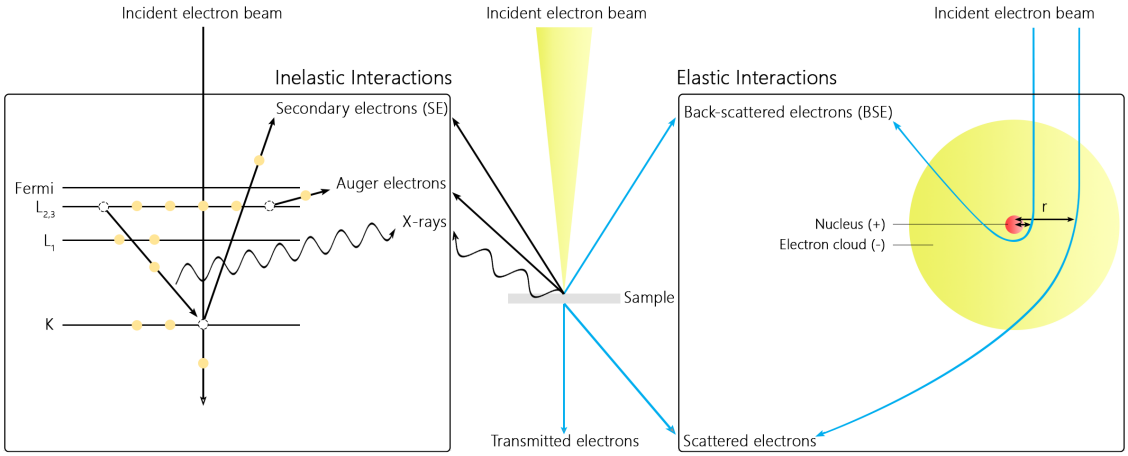

Figure 2.4: A schematic overview of possible electron interactions in an electron microscope. The black arrows represent inelastic interactions between the incident electron beam and the sample. The blue arrows are elastic interactions.

$$\vec{F} = \frac{Q_1 Q_2}{4\pi\epsilon_0 r^2} \tag{2.2}$$

This also holds for inelastic interactions, some of which will be discussed. If a highly energetic electron interacts with an atom's electron cloud, it could transfer part of its energy to the atom. If the transferred energy is sufficient, an inner shell electron (in the case of Figure 2.4 the K-shell) could be ionized, yielding a fast secondary electron (SE). The ionized electron leaves a hole behind in the inner shell, which is an energetically unstable configuration. An electron from an outer shell ($L_{2,3}$) decays into this hole, causing it to lose energy. This energy difference is accompanied by either the emission of a characteristic X-ray (of equal energy to the difference in energy of the K- and $L_{2,3}$-shell) or it could ionize an electron from an outer shell; an Auger electron. The X-ray holds element specific information which can be exploited by Energy Dispersive X-ray Spectroscopy (EDX), but also the Auger electron can be utilized (if it is ejected near the sample's surface) by

means of Auger Spectroscopy. Slow SE's can be obtained if the energy surplus of the incident electron is small. This energy difference could ionize electrons from an outer shell, which have a small threshold energy. As their energy is small, so is their velocity. Alongside BSE's, SE's are used to form a SEM image.[36]

Experimental section Scanning electron microscopy images were recorded on two electron microscopes: A FEI Helios nanolab 600 DualBeam microscope and a PhenomPro X microscope. The FEI Helios nanolab 600 DualBeam microscope was operated at 2.00 kV at a current of 25 pA. All images were formed by secondary electrons with a 3 μs dwell time. The PhenomPro X microscope was equipped with a CsB filament and operated at 10 kV. The single crystal samples were supported on carbon tape deposited over Al stabs (FEI stabs) and inserted in the microscope vacuum chamber without Au coating.

2.1.3 Confocal Raman Microscopy

This technique is a combination of confocal microscopy and Raman spectroscopy. By combining a microscope with a Raman spectrometer, one obtains spectral information with spatial resolution in the XY-plane (Z-axis being the beam direction). Additionally, if the microscope is a confocal microscope, spatial resolution along the Z-axis is also possible. The theoretical frameworks of these characterization techniques is described below.

Raman spectroscopy

As mentioned before, Rayleigh scattering is the elastic interaction of light with matter. This entails that the incident light and the reflected/scattered/diffracted have the same energy. The inelastic interaction between light and matter is accompanied by an energy exchange and is called Raman scattering. This in turns means that the scattered light has either a shorter (anti-Stokes) or longer wavelength (Stokes) than the incident photon. The Raman signal is typically very weak (one in ten million photons is inelastically scattered), therefore the use of strong lasers and sensitive detectors is required. A Jablonski diagram such as Figure 2.5a displays the different kinds of scattering and their respective corresponding energies.[37]

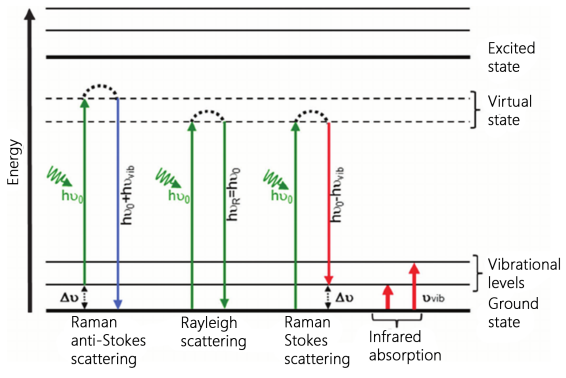

(a) Four transitions are displayed in this Jablonski diagram. Raman scattering and infrared absorption can be exploited to probe the vibrational levels of a molecule. Modified from Baker et al.[38]

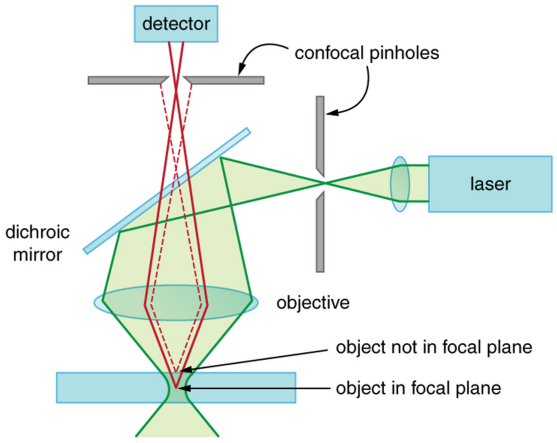

(b) This scheme illustrates the light path in a confocal microscope. The two pinholes filter light originating from other sources than the focal plane. The dashed line is eliminated. Reproduced from [39].

Figure 2.5: The two principles of confocal Raman microscopy.

The degree to which the scattered light's wavelength has changed is called the Raman shift with units of reciprocal centimetres (cm^{-1}). This Raman shift is caused by the various vibrational modes of a bond in a molecule. However, one does not directly measure the vibrational frequencies but rather a consequence of these vibrations. Periodic vibrations cause either a periodic change in magnetic dipole moment or a periodic change in polarizability of the bond. The former is probed in infrared spectroscopy (this will be discussed in Section 2.1.4) whereas the latter is the cause for the signal in Raman spectroscopy. As each measured signal is a characteristic property of a certain bond, one is able to infer molecular information from a sample.[40]

This technique entails many challenges and trade-offs for optimal signal quality. One of the biggest challenges in Raman spectroscopy is the low cross-section. As mentioned earlier, only one in ten million photons is scattered inelastically, therefore high power photon sources (lasers) are required. Furthermore, Raman scattering is also heavily dependent on the incident wavelength. The degree to which Raman scattering is dependent on these two parameters is mathematically described by Equation (2.3).

$$I_{Raman} \propto \left(\frac{\delta\alpha}{\delta q}\right)^2_{q0} \cdot (\omega_0 - \omega_q)^4 \cdot E_0^2 \tag{2.3}$$

On the one hand, Raman intensity[v] is proportional to molecular properties such as $\left(\frac{\delta\alpha}{\delta q}\right)^2_{q0}$ and ω_q which respectively represent the change in polarizability (α) with respect to a vibrational mode (q) and the molecular vibration frequency, ω_q. On the other hand, experimental parameters influence the intensity, namely the laser power (or more accurately, the amplitude of the light's electric field), E_0^2, and the excitation frequency, ω_0. As can be seen, the Raman intensity is greatly dependent on the laser power (second order of magnitude) and excitation wavelength (fourth order of magnitude).[40]

However, simply utilizing extremely high powered lasers with very short wavelengths will not result in the best Raman spectrum. High powered lasers could damage the sample and consequently increasing the noise level. Furthermore, short wavelengths can prove to be inconvenient as besides Raman scattering, fluorescence also contributes to the signal. The efficiency of fluorescence is roughly six orders of magnitude larger than Raman scattering and should be minimized for high quality spectra. As many samples show stronger fluorescence at shorter wavelengths it would be sensible to excite with longer wavelengths. This trade-off between Raman intensity and fluorescence intensity can be troublesome, therefore a careful choice of excitation wavelength is paramount.

Confocal microscopy

Confocal microscopy is a microscopy method in order to filter out of focus light originating from a sample. This is achieved by means of optics and pinholes in the beam path. A simplified set-up is depicted in Figure 2.5b and works as follows. A laser is passed through the first pinhole for it to approximate a point source. This divergent beam path is directed via a dichroic mirror[vi] towards a magnification objective which converges the light bundle on the sample. Subsequently, the focused laser light irradiates the sample resulting in scattered or fluorescent light. This light is in turn passed through the dichroic mirror towards the second pinhole which eliminates out-of-focus light[39].

[v] This description actually represents the Stokes scattering intensity. This can be seen from the negative sign between ω_0 and ω_q as Stokes scattering is always red shifted with respect to the excitation frequency. Mathematical descriptions for Rayleigh scattering do not include a ω_q term as there is no change in frequency. Anti-Stokes scattering is always blue shifted, therefore it contains a $\omega_0 + \omega_q$ term.

[vi] A dichroic mirror is in essence a wavelength filter. For this purpose it is supposed to reflect the wavelength of the incident light whereas other wavelengths are passed through. This type of equipment is typical for fluorescence and Raman measurements, as the incident light and signal light are of a different wavelength.

This is the very essence of confocal microscopy; as the incident light excites parts of the sample outside of the focal plane, the resulting out-of-focus scattering would contribute to the total signal. A pinhole eliminates all contributions except for the light originating from the focal plane, rendering a signal solely comprised of the region of interest. The red lines visualize the light originating from the sample. The full line, which originates from the focal plane, is focused through the pinhole, whereas the dashed line will be blocked. Considering the fact that most of the incident light is blocked, the signal intensity drops drastically. This merits the use of lasers and also extended exposure times. As one is able to change the relative position of the focal plane in the sample, spatial resolution along the Z-axis is possible using this technique[41].

Experimental section All Raman measurements were performed on a Renishaw InVia Raman Microscope, using a 532 nm diode excitation laser with a 20× magnification objective, 1200 lines/mm grating and CCD detector. The 20× magnification objective has a NA of 0.4 resulting in a $6.65\exp(-5)$ cm diameter spot size. All measurements were performed using 1% laser power (0.44 mW) and the Raman shift was scanned statically from 1500 cm^{-1} until 2300 cm^{-1}. Atmospheric control was achieved by measuring the samples enclosed in a microscope stage by Linkam Scientific using a CaF_2 window as is depicted in Figure 2.6. Additional settings such as exposure time and accumulations differ per experiment and will be presented per case.

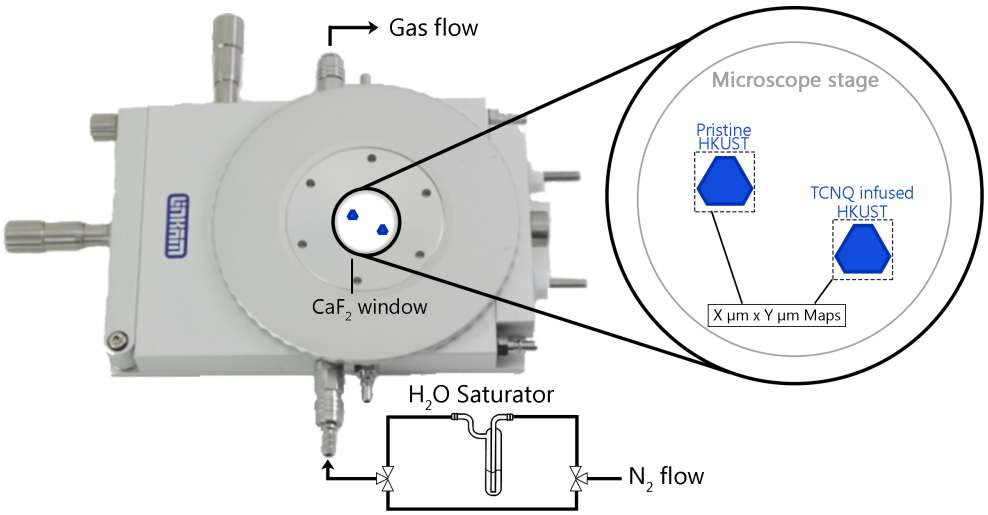

Figure 2.6: This scheme represents the set-up utilized for Raman microscopy and FTIR microscopy measurements. Atmopheric control is achieved by enclosing the samples in a microscopy stage and operating the three-way valves at the H_2O-saturator. The CaF_2 window is IR-transparent.

2.1.4 *In situ* infrared microscopy

IR spectroscopy

Complementary to Raman microscopy, infrared microscopy is the combination of an infrared spectrometer and a microscope in order to obtain spectral information with spatial resolution. More precisely, Fourier Transform InfraRed (FTIR) spectroscopy is a vibrational spectroscopic technique where molecular vibrations can be probed. These vibrational transitions are displayed in Figure 2.5a. In contrast to Raman spectroscopy where a single excitation wavelength is utilized, infrared spectroscopy utilizes a wide spectrum of frequencies. These frequencies often range from the Near InfraRed (NIR), or 8500 cm^{-1}, until 350 cm^{-1} in the Far InfraRed (FIR) depending on the equipment being used.

All molecular vibrations have an energy associated with them and can be assigned to certain quantized levels. Once matter is irradiated with infrared light, the matter could absorb an infrared photon and a transition between vibrational states is induced. The spacing of these vibrational states depends on the vibrational frequency of the bond. Hence, only a photon with a frequency matching that of the vibration frequency can induce the transition of that particular bond. Furthermore, the vibration must induce a periodic change in magnetic dipole moment. As all bonds have a characteristic vibration, one is able to deduce chemical information from a sample by irradiating a sample with photons of a various frequencies and monitoring all induced transitions. Classically, one would irradiate the sample with all frequencies successively and catalogue those frequencies at which a vibrational transition occurs. But since the introduction of the Michelson interferometer, one is able to irradiate the sample with all frequencies at once. This requires processing of the interferogram (which resides in the length dimension) using a Fourier Transform to an absorption spectrum (which resides in the reciprocal length dimension). As all functional groups have characteristics vibration frequencies, the absorption spectrum is utilized to determine the presence of certain moieties.[42, 43]

Optical microscopy

As opposed to confocal microscopy, the IR microscope does not allow for spatial resolution along the Z-axis. This is partially due to the use of suitable optics (as depicted in Figure 2.5b), but also the fact that the obtained signal in IR microscopy is different from that of Raman microscopy. As mentioned earlier, in Raman microscopy the sample is excited by a laser and the emitted light forms the signal. The laser is able to protrude into the sample, exciting many parts of the sample as it does so, yet only emission from the sample's region of interest is collected due to the use of suitable optics. However, for IR microscopy, light of higher wavelengths is used, which lacks the energy to induce electronic excitation. Furthermore, the infrared light is not able to protrude into the sample, as it either reflects of the surface, or is absorbed by the sample just below the surface. These phenomena, reflectance or absorbance, are probed using this technique, as opposed to counting emitted photons which is the case for Raman microsocopy.

This prevents the use of confocal microscopy, yet it does allow for faster signal acquisition. Considering the low cross-section of Raman microscopy, *in situ* experiments are virtually impossible as the time resolution would be very crude. However, the absorption process of infrared light is more efficient, allowing for *in situ* measurements.

Experimental section All measurements were performed using a Perkin Elmer Frontier MIR/FIR Spectrometer as IR source coupled to a Perkin Elmer Spotlight 400 FT-IR microscope. Atmospheric control was achieved by measuring the samples enclosed in a microscope stage by Linkam Scientific using a CaF_2 window as is depicted in Figure 2.6. A Mercury-Cadmium-Telluride (MCT) detector in a 16x16 array of 6.25 μm x 6.25 μm pixels was used. All infrared measurements were the collection of various maps over time under different atmospheres. Temporal resolution was obtained by the acquisition of consecutive maps of the same locations. Scanning occurred in N_2-atmosphere and the crystals were hydrated for 30 seconds in between scans as is depicted in Figure 2.7. By doing so, no further hydration occurs during a scan. As far as temporal resolution is concerned, this strategy renders each scan effectively instantaneous. Spectral resolution differs between experiments, as it affects the temporal resolution, and will be stated per experiment. Analysis was performed by means of home-build scripts and Perkin-Elmer provided scripts in Matlab R2017b by Mathworks. The collected data's format was in a similar fashion to the Raman measurements as a Blockfile; these are conceptually visualized in Figure 2.11. Single-wavelength intensity maps were generated by means of Matlab.

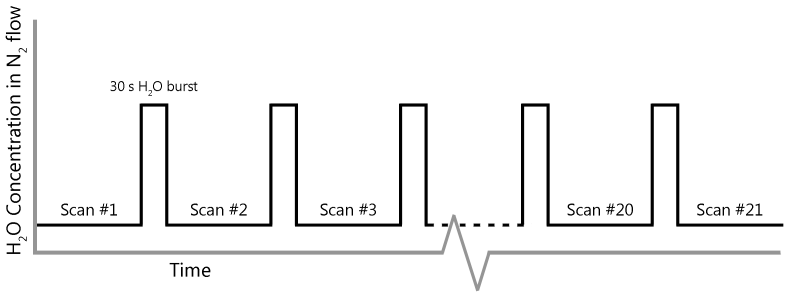

Figure 2.7: This program describes the atmospheric conditions during the FTIR microscopy measurements. Each scan consists two maps under N_2 atmosphere. In between scans the entire stage was hydrated for 30 seconds. This way each scan occurs while the hydration is 'paused' rendering the scan effectively instantaneous.

2.2 Materials

For all spectroscopic experiments, four sample types were utilized. All of them were the MOF HKUST-1 but either powdered or as larger crystals (100 μm - 1 mm) and either pristine or infused with 7,7,8,8-tetracyanoquinodimethane (TCNQ). The synthesis of both materials will be discussed below.

2.2.1 Pristine HKUST-1

Due to the limited spatial resolution of IR-microscopy, large (mm-range) HKUST-1 crystals were grown by means of a nonsolvothermal synthesis reported by Tovar et al.[44] Additional to most syntheses of HKUST-1, acetic acid was added as a modulator. This reagent forms acetate complexes which compete with secondary building units, generating few large crystal instead of many smaller crystallites. This allows the slow but steady growth of large crystal, easily controlled by synthesis time as depicted in Figure 2.8

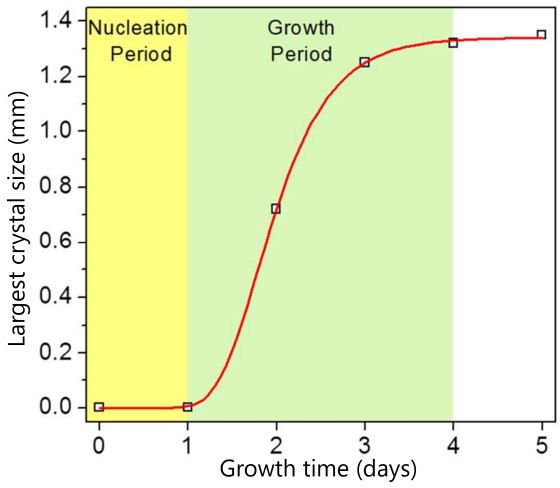

Figure 2.8: This graph represents the growth periods of the nonsolvothermal synthesis of HKUST-1. By adding acetic acid larger crystals can be obtained by tuning the growth time. Reproduced from Tovar et al[44].

In three separate batches, 0.49 g of the copper precursor, $Cu(NO_3)_2 \cdot 3\,H_2O$ (Sigma-Aldrich), was dissolved in 3 ml deionized water and 3 ml dimethylformamide (Alfa Aesar). In three other batches, 0.24 g benzene-1,3,5-tricarboxylic acid (H_3BTC Sigma Aldrich) was dissolved in 3 ml ethanol (Acros Organics) using a heating gun. The vials were combined yielding three batches and 12 ml acetic acid (Acros Organics) was added to each vial. All vials were brought into an oven for 3 days at 55°C.

After three days navy blue crystals were found on the bottom and edges of the vials. Ethanol was added as a washing step and after one day renewed. Two days later, all liquid ethanol was decanted and the crystals out gassed *in vacuo* at $\approx$ 120°C for 20 hours. All crystals were stored in argon.

2.2.2 TCNQ infused HKUST-1

The synthesis for the TCNQ infused HKUST-1 crystals was the same for the pristine HKUST-1 crystals up until the washing step with ethanol. After the crystals were soaked in ethanol, a solvent exchange step followed as the crystals were submerged in dichloromethane for several days. During the solvent exchange step the dichloromethane was renewed five times. Subsequently the crystals were activated by desolvating under dynamic vacuum at 180°C overnight. The crystals were brought into a glass ampoule with an excess of $TCNQ/CH_2Cl_2$ saturated solution (approximately a 2 equivalents of TCNQ for 1 formula unit Cu_3BTC_2). The ampoule was subsequently out gassed, flame-sealed and placed in an oven for one week at 180°C.[44]

2.3 Analysis

As Raman microscopy yields large datasets, principle component analysis in combination with K-means clustering was performed in order to locate certain spectral features on the sample. The underpinning principles of this process is described below.

2.3.1 Principle Component Analysis (PCA)

For large multivariate datasets, many samples are often correlated by many variables. In turn, some variables are more relevant than others and certain variables could be correlated to each other. This renders the interpretation of large datasets not straightforward and valuable information could be overlooked. Principle component analysis is a multivariate statistical procedure to gain information on the relevance of variables. As one is able to discern the relevance (or consequence) of all the variables, it is possible to either eliminate or give prominence to certain variables. This seems rather conceptual, but in essence PCA enables the reduction of the dimensionality of large datasets, without sacrificing (too much) information. This renders a more insightful dataset, reducing the chance to overlook important features.[45, 46]

For example, if two properties (height and weight) of a hundred people were plotted, a useful way in doing so is by means of a scatter plot, with weight on the abscissa and height on the ordinate. This 100x2 dataset would be visualized as an ellipsoid along the diagonal of the graph. This situation is depicted in Figure 2.9. Even though this bivariate dataset is simpely interpreted, it is possible to reduce the dimensionality of this dataset (100x2) to only one variable (100x1) without sacrificing (too much) information. This is achieved by projecting the dataset along a direction which maintains maximum variance. In this case, this would be the diagonal of the graph and is called the first Principle Component (PC). One could consider this new axis as the 'size' dimension, which holds information both on height and weight. Consider the fact that in interpreting the original dataset, the distance of each point *along* this diagonal direction is more relevant than the distance *from* this diagonal. Therefore, by choosing this direction as the diagonal of the graph, variance is maximized. After projecting each point on this new diagonal axis, only the information of the distance *along* the diagonal is preserved, while losing information of the distance *from* the diagonal. However, as the distance from the diagonal is of less relevance, only little

information remains undescribed, yet the original dataset has reduced in dimensions, rendering it easier to interpret. One could determine the second PC, as long as both PC's are mutually orthogonal. This second PC would describe the remaining variance (which is substantially less than the first), so one could choose to eliminate this second PC entirely. Granted, this example was easily interpretable from the start, but this procedure also holds for large multivariate and covariant datasets which do require simplification before they become insightful.

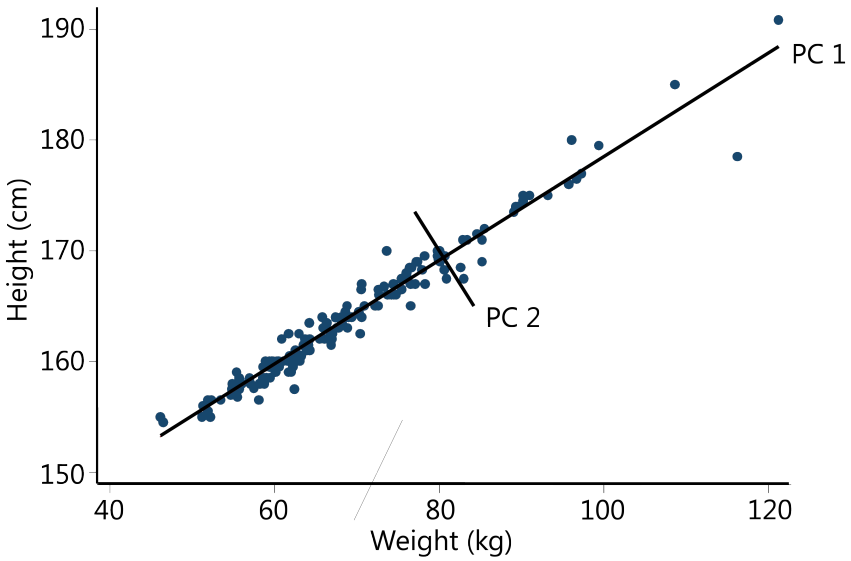

Figure 2.9: The dimensionality of this examplary dataset can be reduced by means of PCA by eliminating the less descriptive of the 2 PC's.

Without diving too deep into the mathematics behind PCA, it is useful to describe how a PC is calculated. A PC is actually one of the eigenvectors of the covariance matrix of all the variables. Therefore, there are as many PC's as there are variables. This would imply that there would be no reduction of the dataset's dimensionality as the amount of PC's is equal to the amount of variables. But given the fact that the described variance per PC declines for each successive PC, one could choose to eliminate the PC's as soon as the cumulative variance has reached a desired amount. Therefore the PC's can be considered as new 'more fundamental' variables which are, due to their mutual orthogonality, uncorrelated and also fewer in number than the original variables.[47, 48]

There are various methods to determine whether enough PC's describe sufficient cumulative variance. Amongst many, the 'Scree test', 'Cumulative variance explained' and 'Eigenvalue below one' will be described. These methods are based on the fact that PC's become less important as their number increases. As this is an inherent quality of PC's, these techniques either assess their importance by means of logical reasoning or by mathematics.

The Scree test plots each PC versus its eigenvalue[vii], as can be seen in Figure 2.10. As contributions of relevant signal are more important than random noise, the eigenvalues of relevant signal should be high as the magnitude of their variance is high. Consequently, the eigenvalues of noise are small and should show a very gradual decline as the number of PC's increase. If one were to plot the total of eigenvalues versus number of PC's there will be a 'knee' or inflection point in the plot. The PC's before this knee have large eigenvalues and therefore describe relevant signal. After the knee mostly noise is described, which in turn means that these PC's describe less

[vii]The cross products of the data of the covariance matrix.

relevant fractions of the data. This approach is analogous to the cumulative variance explained (CVE) method. This plots the cumulative variance explained versus the number of components. As soon as the decreasing ascending plot levels off, PC's will describe less relevant data and should be disregarded.

The eigenvalue below one method also plots the eigenvalue versus the number of components (Figure 2.10). In the case of autoscaled data, each variable's variance is unity. If each variable would be uncorrelated (and therefore orthogonal), the resulting PC's would all have an eigenvalue of one. This in turn yields a correlation matrix as the identity matrix, which renders PCA rather obsolete as each PC only describes one variable. However, if variables were correlated (as usually is the case), PC's would have an eigenvalue greater than one and therefore represent more than one variable. This is what PCA aims to achieve, describing several variables as one 'fundamental' variable, the principle component. So, the eigenvalue below one methods aims to plot all PC's with an eigenvalue greater than one, and therefore distinguishing the PC's that describe all variables from the PC's that do not. This grants insight in the amount of PC's required to describe a desired amount of cumulative variance. Ambiguously, not all tests will provide the same amount of required PC's. This implies that one can not follow these tests blindly, as they merely give an indication at which information becomes less relevant. As in the end, PCA is a mathematical means to simplify data. Therefore, one has to be cautious of whether one views actual chemical information, or mathematical constructs.

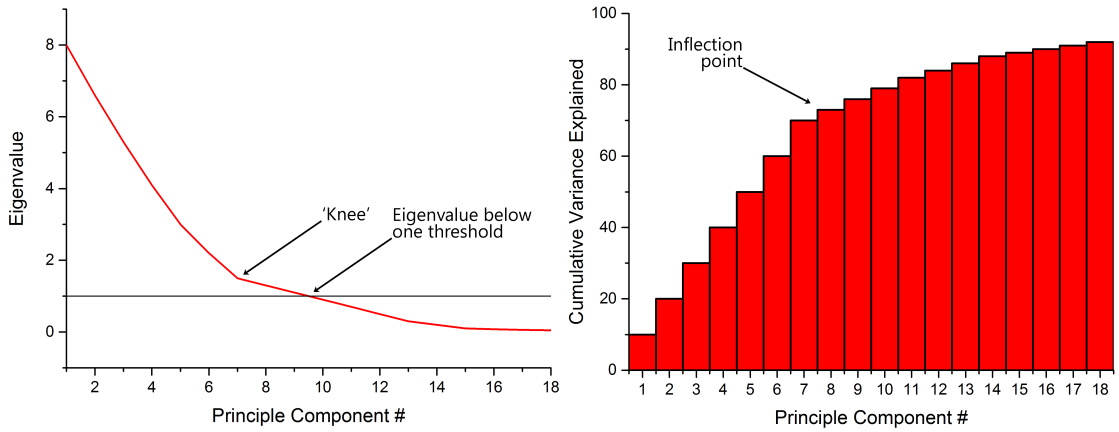

Figure 2.10: These methods assess the right amount of PC's required to explain the desired amount of variance. On the left the scree test and eigenvalue below one are depicted. According to the scree test, the point at which PC's become less relevant is at the 'knee'. The point at which the eigenvalue are below zero is another point at which PC's become redundent. On the right is the CVE plot. This shows an inflection point after seven PC's.

When one performs the PCA procedure, there are several quantities to consider. Especially, the original data matrix, the loading vectors, the score vectors and the residuals matrix. The relation of these matrices is graphically depicted in Figure 2.12. In order to illustrate this, a prototypical dataset obtained by Raman microscopy will be used as an example. The original dataset has m x n pixels (a square map, referred to as M samples for convenience), with each pixel comprisied of a Raman spectrum of W wavenumbers (or variables). These so-called 'Blockfiles' are conceptually visualized in Figure 2.11. This yields an M x W dataset of which PCA would generate W principle components. Each principle component is comprised of M scores (eigenimages) and W loadings (eigenspectra). The loading defines what the PC actually represents. As a PC is a linear combination of the wavenumbers describing a sample, a PC's loading describes which wavenumbers are considered more or less relevant for the particular PC. For simplicity's sake one could regard the loading as the qualitative part of the PC. In addition, the scores of a PC

define to what degree (or how much) the loadings represent each sample. Or less conceptual: the quantitative part of a PC. The residuals have the same structure as the original dataset and hold information on the explained and unexplained fractions of the variance. There will be no further explanation on the residuals as their purpose is not important for this case.[49]

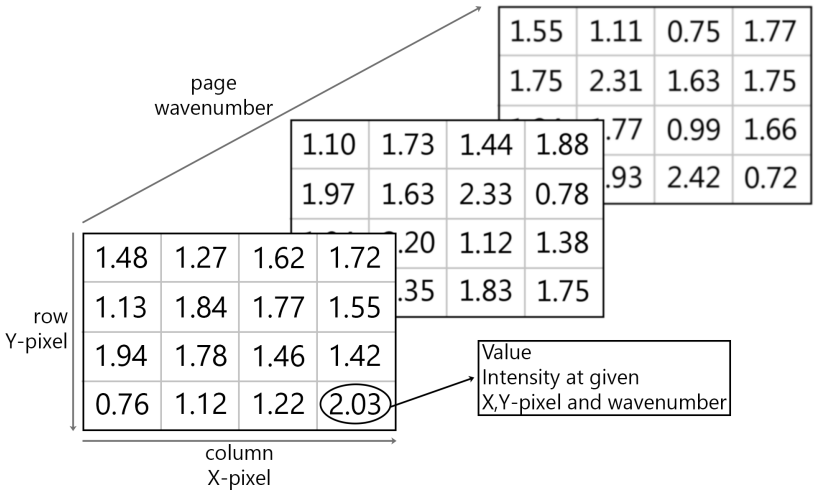

Figure 2.11: A multidimensional array (4x4x3) or Blockfile in which the rows correspond to X-pixels, the columns correspond to Y-pixels and the pages correspond to wavenumbers.

A quick example could make this more intuitive. A spectral dataset of 2 samples with peaks at 1500 cm^{-1} and 1800 cm^{-1} is explained by various PC's. The first two PC's loadings depict a high relevance of the 1500 cm^{-1} peak but a low relevance of the 1800 cm^{-1} peak. This description is a qualitative one as it is given by the PC's loadings. However, the first two PC's scores are different, namely the scores of the first PC are positive and negative for the second PC. This means that for the first PC the 1500 cm^{-1} peak is a more 'essential' part of the signal whereas the 1800 cm^{-1} is not. The second PC however had negative scores, which inverts the relation, rendering the 1800 cm^{-1} peak more 'essential' than the other peak.

Usually, there are many samples and many variables, therefore there often is no straightforward relation as the one stated above. These relations are more clearly explained by certain trends which can be recognized by means of K-means clustering. Subsequently, these clusters have a spatial coordinate, which renders them very useful in determining the location of certain spectral features on the sample.

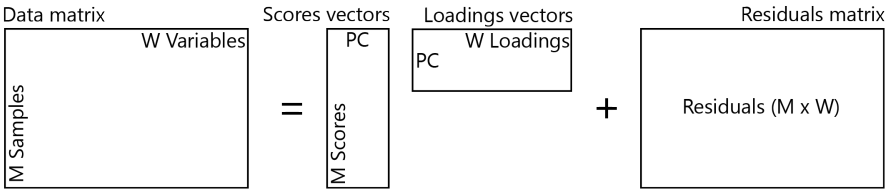

Figure 2.12: The four quantities that described the PCA procedure. There are as many PC's as there are variables. Subsequently for each PC, there are as many scores as there are samples and as many loadings as there are variables. The unexplained fraction of the variance is represented by the residuals matrix and has the same structure as the original data matrix.

K-means clustering is the next step in the signal processing procedure. The clustering analysis aims to group samples (pixels in this case) which have comparable spectral qualities. By plotting the scores of two PC's against one another as a scatterplot, one is able to group various scores that lie in each others proximity. Consequently, the samples that fall within a group are bound to have common spectral features.

This process works by grouping the samples in Voronoi cells[viii]. The amount of Voronoi cells (K) has to be set *a priori* and is chosen based on the expected variation of spectra. This is a heuristic method as the amount of clusters could be tuned if the clustering shows overlap or if there is too much variance within the clusters.[50–53] As mentioned earlier, the clusters are generated based on their spectral similarity. This enables the visualization of pixels with similar spectral features and therefore possible heterogeneities within the sample.

Additional to K-means clustering, another procedure can be performed in which clustering is based on Gaussian Mixture Models[ix] (GMM). In contrast to K-means, which clusters data points based on their mean Euclidean distance to a seed, GMM clustering is based on Gaussian distribution functions, which incorporate the covariance of the data. This is useful as K-means clustering merely describes circular clusters and fails to recognize overlapping clusters. In order to determine whether each data point is actually described best by which Gaussian distribution function, Expectation Maximization (EM) for GMM is performed. EM for GMM is an iterative procedure in which Gaussian distributions are fitted to the data points. Subsequently, the normalized probability of whether each data point belongs to a certain distribution is computed. For each following iteration, the Gaussian distributions are replotted for maximum probability until convergence is achieved.[54–56]

Experimental section Data analysis was performed using WiRE 3.4 software by Renishaw and Matlab R2018a software by Mathworks. Maps were collected of various pixel sizes with each pixel representing a Raman spectrum. A peak of interest was selected and either an absolute intensity or signal to baseline value was obtained for each pixel. Pseudo-color plots, which represent single-wavelength (relative) intensity plots, were generated using Matlab. Cluster analysis was performed in order to visualize possible crystal heterogeneities. These clusters were determined by means of principle component analysis.

[viii] Voronoi cells are the partitions of a plane based on Euclidean distance between 'seeds' within a set of samples. The amount of seeds is set beforehand (and eventually equal to the amount of Voronoi cells) and all the samples are grouped to the seed which is closest to it. This results in clusters containing samples where variance is minimized (i.e. where the similarity between samples is maximized).

[ix] A mixture model is a statistical model in which the existence of subgroups in an overall group is represented based on probability. An exact description of this statistical model would be beyond the scope of this thesis. But in essence it is the description of how various probability distributions of random variables are convoluted (subgroups convoluted in an overall group). In the case of Gaussian Mixture Models, the probability distributions are Gaussian distributions, in which the mean and covariance are accounted for.

Chapter 3

Dehydrated State

Initially, the distribution of TCNQ over the single crystals is assessed by means of confocal Raman microscopy, which is described below. The data will be analysed in its raw form with no alterations (single wavelength intensity maps) and also after processing the data using PCA.

3.1 Confocal Raman microscopy

Two crystals are investigated to find the distribution of TCNQ over the crystals. To this end, two Raman active vibrational modes of the TCNQ molecule are monitored: the aromatic C=C stretch at 1605 cm^{-1} and the C≡N stretch at 2226 cm^{-1}. Especially the first vibrational mode is accompanied by some complications as the vibration is also present in the the organic linker (benzene-1,3,5-tricarboxylic acid). The latter vibration is exclusively present in TCNQ, which should provide a clear distinction between the two contributions at 1605 cm^{-1}.

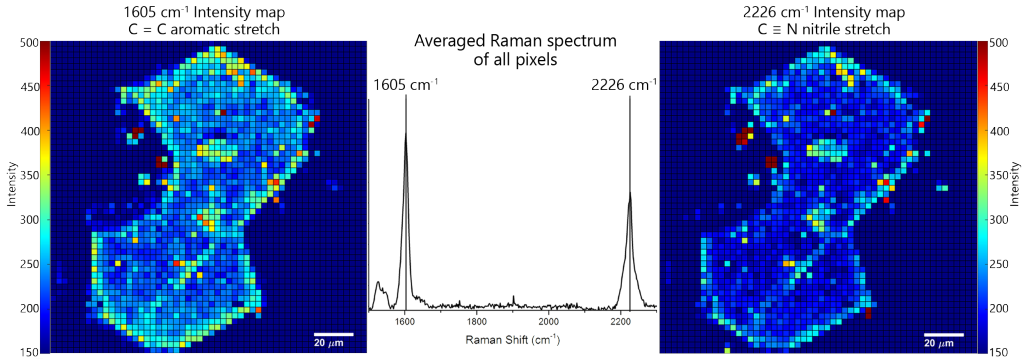

Figure 3.1: Left: Single wavelength intensity map at 1605 cm^{-1}. Middle: The average Raman spectrum of all pixels. Right: Single wavelength intensity map at 2226 cm^{-1}.

Figure 3.1 depicts the results of the Raman imaging experiments on the dumbbell-shaped crystal. The average spectrum of all pixels in a 54 x 54 rectangular map is acquired and four peaks can be discerned. A minor peak at 1525 cm^{-1} which represents the assymetric C–O_2 vibration of the organic linker.[57] Furthermore, a very small contribution at 1900 cm^{-1} which is due to a cosmic ray of two pixels. These pixels are depicted in the second principle component of Section A.1. The intensity of cosmic rays is generally extremely high, yet it has diminished as it is averaged out. The major contributions are at 1605 cm^{-1} and 2226 cm^{-1} which are from the aromatic C=C stretch (of both the organic linker and TCNQ) and the C≡N stretch of TCNQ, respectively.[22] Of these two contributions, single wavelength intensity maps are rendered and certain regions of increased intensity are clearly visible. The map at 1605 cm^{-1} clearly

outlines the general shape of the crystal with elevated intensity around the edges. The maps suggests the presence of the C=C stretch throughout the crystal, which is expected as the linker is assumed to be evenly dispersed. Considering that intensity scales with concentration of a vibration, the map implies that the areas with elevated intensity around the edges is due to the accumulation of contributions of the organic linker and the TCNQ molecule. As the same contrast in intensity is found in the single wavelength intensity map at 2226 cm^{-1}, it could signify an elevated concentration of TCNQ around the crystal edges.

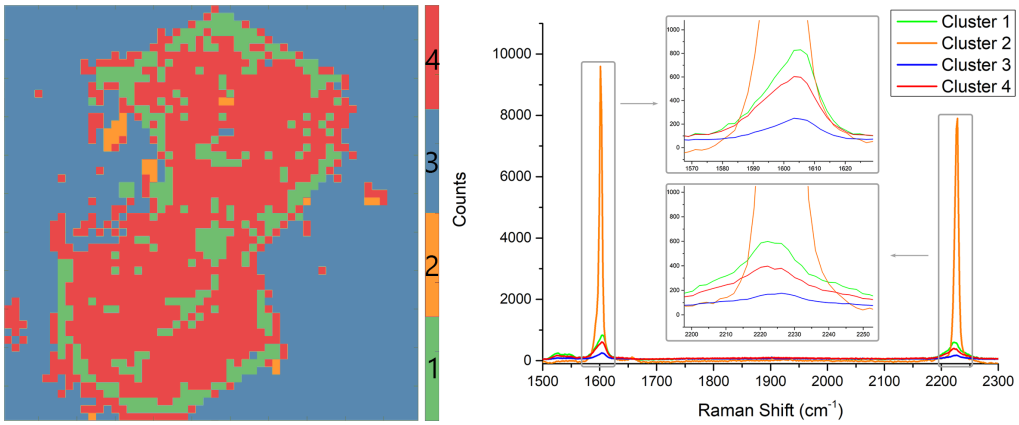

Figure 3.2: The principle components analysis results of the Raman imaging experiments. Four clusters are generated based on spectral similarities. Cluster 1 (green) is mainly situated at the crystal edge. Cluster 2 (orange) is visible as several 'hotspots' with very high intensity. Cluster 3 (blue) represents the background and cluster 4 is found at the crystal centre. On the right the corresponding (averaged over each cluster) spectra are depicted.

Principle components 1, 3 and 7 are chosen for the K-means clustering analysis. These components are chosen based on their cumulative variance explained and on examination of the eigenimages and eigenspectra. Further justification, CVE, eigenimages and eigenspectra are given in Appendix Section A.1.

The clustering analysis yields a clustermap with four distinct regions of similar spectral information. The spectra per cluster show that each cluster holds the same spectral features, namely the peaks at 1605 cm^{-1} and 2226 cm^{-1}, yet there is a clear difference in relative intensity. As these spectral contributions originate from all over the sample, spatial heterogeneities are mostly to be observed as relative intensity differences. This implies that chemical moieties are to be found throughout the crystal, though in some regions in elevated concentration.

The background is easily recognizable as the blue cluster 3. The corresponding spectrum does show some intensity at 1605 cm^{-1} and 2226 cm^{-1}, yet this is due to cluster merging of true background and very small contributions of far out-of-focus parts of the sample. Another cluster is the orange cluster 2, which is only situated at very distinct regions or hotspots. The associated spectrum of cluster 2 depicts a dramatic increase in intensity with virtually no features at 1525 cm^{-1}, which suggests the presence of condensed and highly concentrated TCNQ. These regions correspond with the same high intensity regions of Figure 3.1.

The same trend can be recognized by the hexagonally shaped crystal as depicted in Figure 3.3. Increased intensity around the edges and a very intense hotspot of condensed TCNQ. This is also confirmed by the associated PCA results.

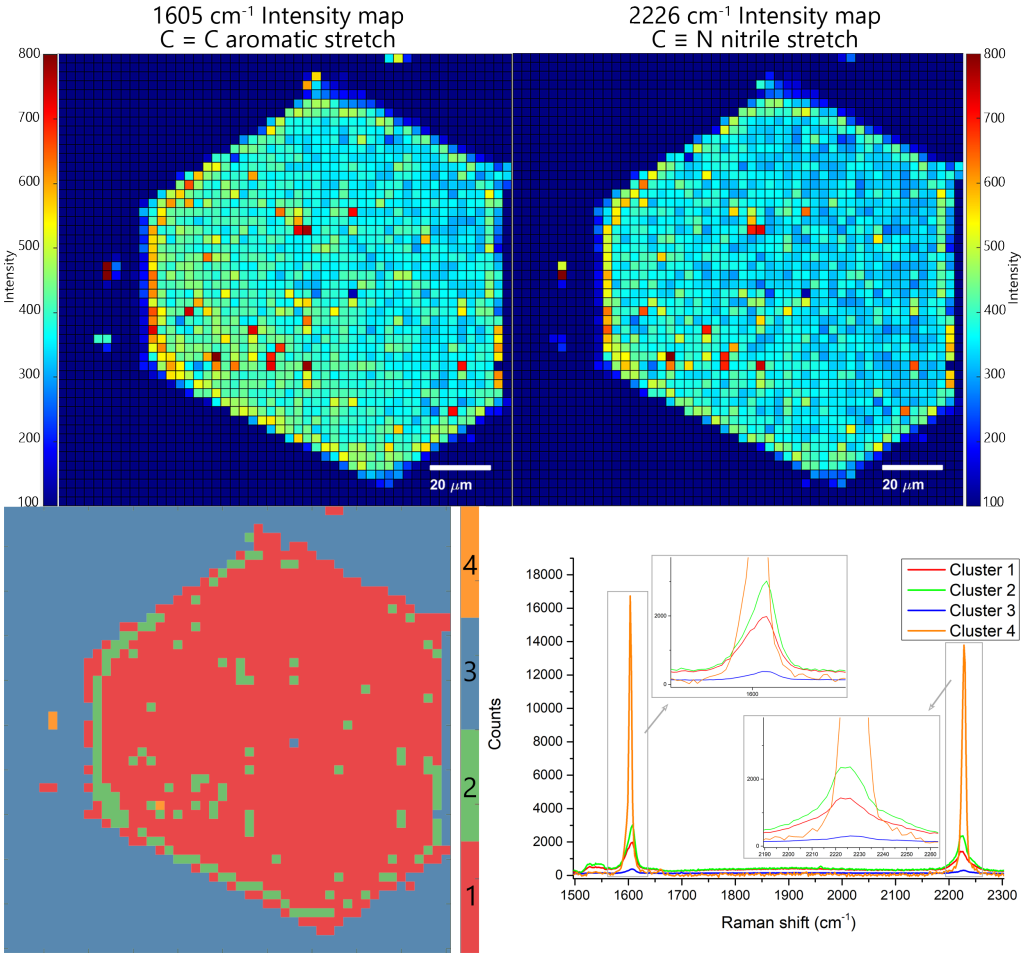

Figure 3.3: All Raman microscopy results of the dehydrated hexagonal crystal. Top: Single wavelength maps of 1605 cm^{-1} and 2226 cm^{-1}. Bottom: PCA and clustering analysis results.

3.2 Conclusion

Over both crystals, similar features are found. Contributions of both 1605 cm^{-1} and 2226 cm^{-1} are found all over the crystal, but the edges presented elevated intensity. These TCNQ enriched regions at the crystal edges can be explained as consequence a of the means of impregnation. As mentioned in Section 2.2.2, the HKUST-1 crystals were impregnated by a solution of TCNQ in CH_2Cl_2. The liquid phase is assumed to migrate inwards towards the crystal centre over time. This causes the crystal edges to be exposed for a longer period of time than the crystal centre, hence the elevated concentration.

Various locations exhibited a dramatic increase in intensity which is assumed to be due to 'hotspots' of condensed TCNQ.

Chapter 4

Dynamic Hydration

The distribution of TCNQ is found to be mainly around the edges. By means of *in situ* IR microscopy the distribution of H_2O will be probed. The conditions of the hydration experiments will be determined by means of *in situ* XRD beforehand.

4.1 *In situ* X-ray diffraction

Before any measurements on single crystal hydration by means of IR microscopy are performed, bulk hydration is performed on powdered HKUST-1 to probe overall stability and sorption qualities. The bulk hydration experiments were monitored *in situ* by X-ray diffraction. As mentioned in Section 1.1.2, the Cu-Cu distance changes upon water absorption/desorption, distorting the octahedral cage. This phenomenon, and stability towards elevated temperatures and prolonged exposure to H_2O will be investigated by XRD.

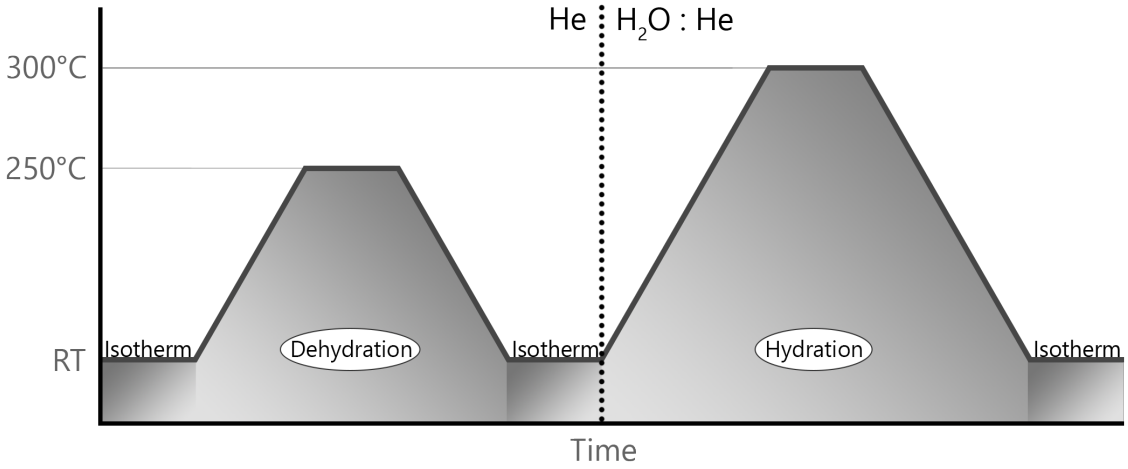

Figure 4.1: The temperature and atmosphere program of the XRD experiment. The sample is initially outgassed in helium and subsequently hydrated in a moisture saturated atmosphere.

The scheme has been devised (Figure 4.1) to monitor HKUST-1's crystallinity under various temperatures and under inert and vapour saturated atmospheres. A powdered sample is used, as spatial resolution can not be acquired and smaller crystallites are beneficial for averaging out the many random orientations the samples can hold during measuring. Furthermore, this also increases the rate of adsorption/desorption as fewer diffusion limitations can occur. The pre-hydrated sample is initially outgassed by heating the sample under helium atmosphere to 250°C

and subsequent cooling. After an isothermal period, the atmosphere is changed to a H_2O vapour saturated helium atmosphere. The sample is reheated to 300°C (assumed to be the limit before thermal degradation) and cooled back to room temperature. During this temperature and atmosphere program, the sample is continuously scanned. The results are depicted in Figure 4.2.

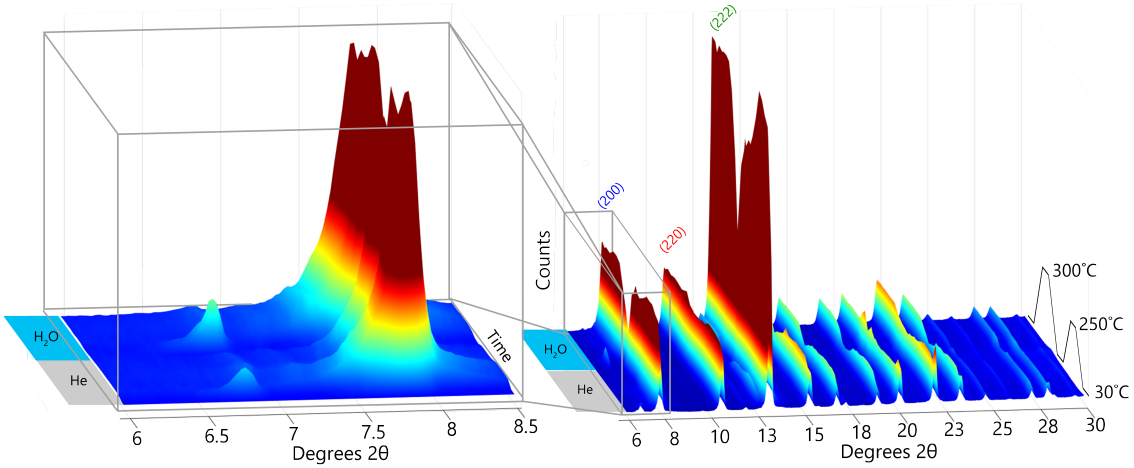

Figure 4.2: *In situ* X-ray diffraction results of the hydration of HKUST-1. The temperature program is depicted on the far right and the atmospheric conditions are depicted on the left of each graph. In the left graph all peaks in between 6 and 8 degrees 2θ are magnified.

The most prominent peaks in the XRD pattern are situated at 7.8, 11 and 13.5 degrees 2θ. These originate from the (200), (220) and (222) planes, respectively, and are commensurate with reference spectra of HKUST-1.[8] However, the change in these contributions over time is what is most interesting. Most features are due to temperature effects. The change in intensity of these three peaks is very similar to the temperature program depicted on the right of Figure 4.2. As for the peak shifts, which are more difficult to observe, they also follow the same trend as the temperature program. From Figure 4.3 one can see that each peak shifts to the right as the temperature increases. This is due to lattice expansion caused by the increased temperature.

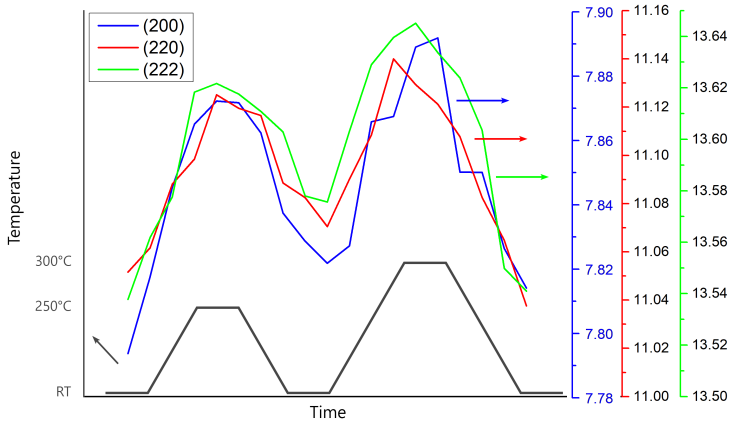

Figure 4.3: In this figure the peak shifts of the three major peaks are visualized. It is clear to see that the peak shifts follow the same trend as the temperature program.

However, besides these changes, the general shape of the pattern is preserved, implying a stable structure with regard to elevated temperatures and H_2O exposure. Although, there is a small contribution at 6.7 degrees 2θ which is present at the beginning of the experiment and just after H_2O is introduced. This small peak is ascribed to a guest molecules binding to metal centres in the pores, which is the exact behaviour one suspects of H_2O.[8] One can see this peak disappearing as the temperature exceeds a certain value at which H_2O is expected to desorb. Furthermore, although it is very minor, at the end of the measurements (where temperatures become ambient again) the intensity at 6.7 degrees 2θ seems to increase ever so slightly.

As for suitable conditions for *in situ* IR microscopy measurements, it was decided that room temperature would be ideal. Besides practical considerations, H_2O desorbs from the structure at elevated temperatures, preventing the possibility to probe TCNQ's stability in H_2O environment.

4.2 *In situ* IR microscopy

Single crystal imaging When identifying spatial heterogeneities, it is paramount that one is able to discern the background contributions from the crystal contributions. The carbon tape onto which the crystal was mounted, contributed significantly to the overall IR signal, obscuring the edges of the crystal. This required preprocessing of the raw data before any further analysis is possible. From examination of the background and crystal spectra, a clear yet noise unrelated difference in absorbance is found at 1372 cm^{-1}. This wavelength is suitable as it was not expected to present any changes during hydration, as opposed to the wavelengths larger than 3000 cm^{-1}. This difference is confirmed by visual examination of 2D intensity maps. Of all IR maps, 16-bit grey-scale .tif images are generated for each wavenumber. Black pixels represent low absorbance for the particular wavenumber and white pixels represent high absorbance. The clearest contrast (i.e. most pronounced difference between background and crystal) is found at 1372 cm^{-1}, confirming the chosen wavenumber as suitable. Typical examples of spectral data and grey-scale .tif images are depicted in Figure 4.4. A mask is defined based on the absorbance of each pixel at 1372 cm^{-1}, by discarding the pixels of which the absorbance exceeds a certain threshold in between the background and crystal absorbances. Relevant MATLAB code is provided in Appendix Section A.2. This renders a clear intensity map of solely HKUST-1 contributions.

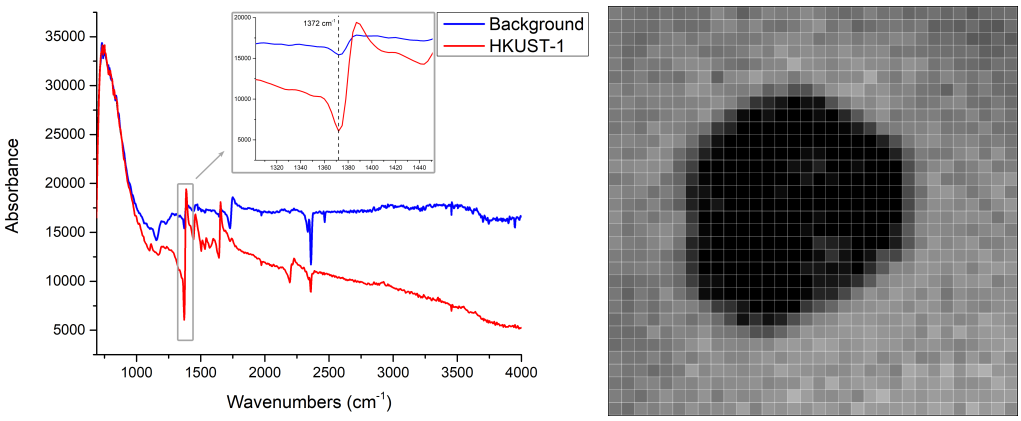

Figure 4.4: Left: A typical spectrum from a crystal pixel and a background pixel. It was decided that the absorbance difference at 1372 cm^{-1} would yield the clearest distinction between crystal and background signal contributions. Right: 16-bit grey-scale .tif image at 1372 cm^{-1}. White pixels represent high absorbance and black pixels represent low absorbance.

Contributions merely from the crystal are readily visualized by applying the mask. After every 30 seconds of hydrating the crystals, maps are acquired and four of which for each crystal are depicted in Figure 4.5. The first map is still in inert conditions and some pre-hydration can be recognized. The edges for both crystals exhibit elevated intensity at 3400 cm^{-1} indicating the presence of either H_2O or remnants of ethanol from the washing steps after synthesis. As the hydration occurs, the overall intensity of all the pixels increases, yet the change around the edges is more pronounced than the centre.

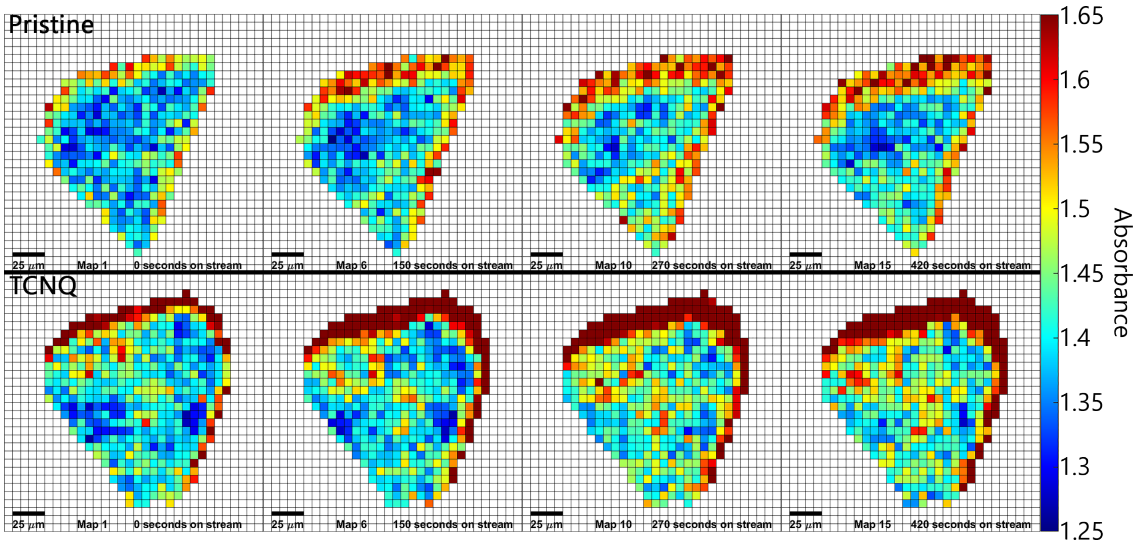

Figure 4.5: Intensity maps at 3400 cm^{-1} of both samples at various time intervals. The hydration is visible as the intensity of especially the edge pixels increases with hydration time.

As mentioned above, the crystal edges exhibit increased intensity compared to the crystal centre. However, one would expect increased intensity over all edges, yet from Figure 4.5 it can be seen that for both samples the most prominent intensity increase is at the top-right edges. This is believed to be due to the positioning of the surface, which is slightly off-perpendicular to the incident light. Certain regions of the surface would therefore lie either slightly above or below the focal plane. In this case, the top-right pixels present elevated absorbance as they are more in focus than the bottom-left pixels.

In the coming section, the absorbance will be plotted as a function of the crystal's radius. The uneven absorbance in the crystal could result in an underestimation. However, as both crystals present the same offset in absorbance[i], comparisons would still be reliable.

The crystal's average absorbance is plotted as a function of the hydration time in Figure 4.6 and a concave down, increasing graph is obtained. This indicates the gradual decline of H_2O uptake up as the crystal becomes saturated. Just by comparing the average absorbance of the entire crystal, both samples are rather similar. Yet the maps of Figure 4.5 indicate that a greater build up of H_2O occurs at the TCNQ-infused crystal. To elucidate the spatial differences in each crystal, further analysis is required.

[i]As the offset is very similar, it is assumed that it is caused by a tilted microscope stage.

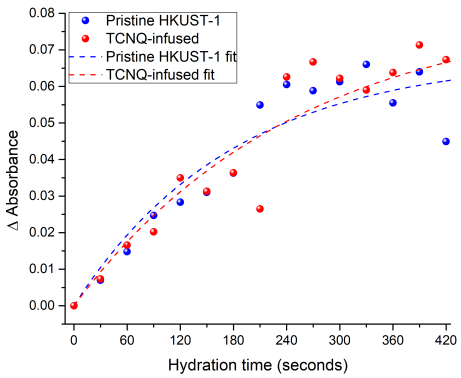

Figure 4.6: Average absorbance values for each entire crystal over time. The concave down, increasing function indicates a gradual saturation of both crystals as the hydration time transpires.

Spatially resolved analysis After the mask has been applied, the absorbance as a function of the crystal's radius is assessed. These graphs could then be compared over time, yielding spatial and temporal information. To this end, an algorithm is devised which indexes pixels as layers in an onion-like fashion. Averaging over the amount of indexed pixels yields an absorbance value at a discrete distances (or layer) from the crystal centre. Subsequently, these values are plotted and an exponential decline as the centre is neared is expected. This is visualized in Figure 4.7. A detailed description of the algorithm and the actual code is presented in Appendix Section A.2. In summary, the algorithm calculates the average absorbance of each layer of the crystal and plots the average absorbances as a function of its corresponding layer. It has to be noted that the layers on the abscissa are denoted as "radius", whereas not the actual radial distance is meant. Each value of the abscissa is a discrete layer of 1 pixel (6.25 μm) thick, with layer 1 representing the surface.

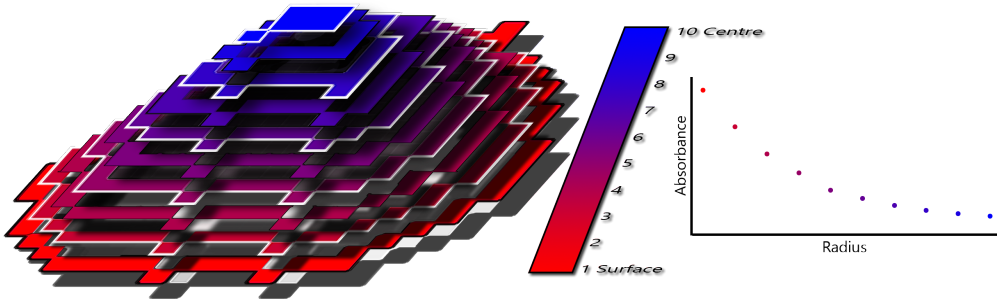

Figure 4.7: This scheme visualizes the approach of the algorithm. Each layer of the crystal is iteratively indexed and the average absorbance per layer is assessed. The subsequent absorbances are then plotted as function of the crystal radius.

The algorithm is applied to the crystals displayed earlier in Figure 4.5 in order to gain further insights into the spatial heterogeneities visualized in Figure 4.5. Each iteration, the outer layer of the crystal is assessed and the average absorbance plotted. The results are depicted in Figure 4.8 and two concave up, decreasing functions are obtained. These plots are plotted as a function of distance, which provides spatial information.

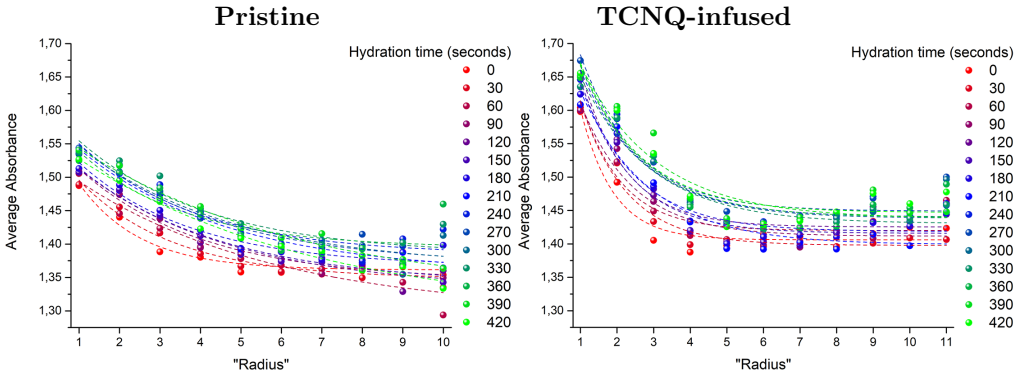

Figure 4.8: The spatial information plots in which the absorbance at 3400 cm^{-1} is plotted as a function of the radius. For both plots an exponential decay is identified which levels off as hydration transpires.

The exponential decline in absorbance is explained as the hydration is expected to decrease as the centre is neared. This trend is found for both samples, yet the TCNQ-infused sample exhibits a steeper decline in the layers 1-4 than the pristine sample. This infers a less gradual concentration of H_2O from the surface to the centre for the TCNQ-infused sample. When viewing the abscissa of the TCNQ graph, there are eleven values whereas the pristine sample only shows ten. This is simply due to the fact that the TCNQ crystal was slightly larger and the algorithm required one additional iteration before all layers are assessed.

Upon close inspection of Figure 4.8, it can be seen that the data points of the early stages of hydration are generally lower in absorbance than the points at the later stage. This is commensurate with the information visualized by Figure 4.6 as it provides the average absorbance of all radial points at a certain point in time. However, as Figure 4.8 points out, the slope of the fits grows less steep as the hydration transpires. This is especially expressed at the layers 2 - 5. The change in slope infers the fact that some layers hydrate at a different rate than others.

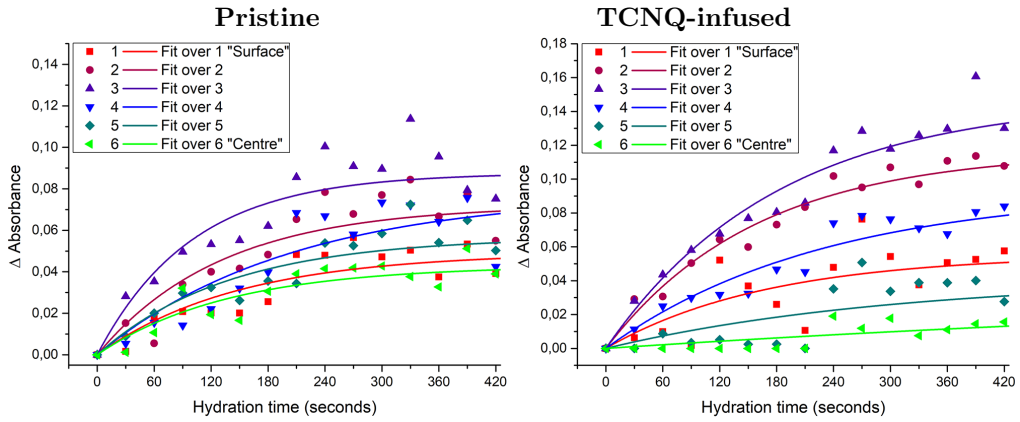

Figure 4.9: The temporal information plots in which the change in absorbance at 3400 cm^{-1} is plotted as a function of hydration time.

Additional to spatial information, by permuting the graph in Figure 4.8 one obtains temporal information per layer. Furthermore, by equating each starting value, the changing slopes are displayed as Δ Absorbance as a function of hydration time. These plots are depicted in Figure 4.9.

Only the plots for layer 1 - 6 are permuted. It has been decided that from layer 7, no more significant changes in absorbance could be identified. The reason for this is twofold. Firstly, the absorbance values of the inner layers are averages of fewer pixels (as inner layers are smaller)

and therefore show larger variation (and standard error). This renders calculations and fitting very troublesome. Secondly, from Figure 4.8, the slopes of the inner layers graphs are virtually horizontal, indicating a very small to negligible response to the hydration. Therefore all layers from 7 towards the centre are considered as a 'continuum' in which no response (during the time frame of 420 seconds) was identified.

The data points of each plot are fitted using a one-phase association function:

$$\Delta\text{Abs} = A\left(1 - e^{-kt}\right) \tag{4.1}$$

in which A represents the maximum Δ Absorbance, t the hydration time and k the rate constant. This model is often used as it describes pseudo first-order kinetics in which a ligand is to associate with a receptor. In this case, H_2O is the ligand which associates to the receptor HKUST-1. The exponent causes the curve to gradually level off as the amount of unoccupied receptors decreases with time until all receptors are saturated and a plateau at value A is obtained. The rate at which the receptors are saturated (or the curvature of the curve) is dictated by the rate constant k, which has units of reciprocal seconds. The physical meaning of this constant is the amount of 'hydration events' per second, or simply put: the rate at which each layer becomes hydrated.

The graphs visualize an initial hydration which is rather fast and gradually declines with time. But optimal comparison is achieved by plotting both A and k as a function of its corresponding layers. These plots are depicted in Figure 4.10. It has to be noted that for the pristine sample data point 4 has been discarded as the fit of layer 4 depicted in Figure 4.9 was very poor.

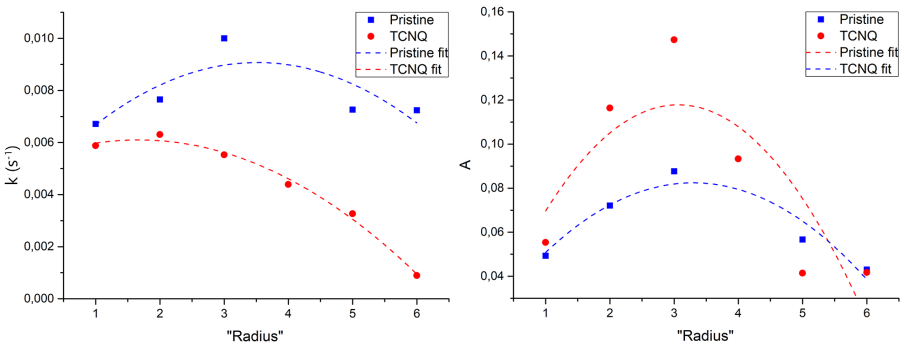

Figure 4.10: Left: Rate constant k vs radius which represents the rate of hydration per layer. Right: Maximum Δ Absorbance vs radius which represnts the amount of hydration per layer.

From Figure 4.10 the true difference between both samples is visualized. From the k vs radius plot, it can be seen that the k-value of the pristine sample shows little decrease or increase. A blunt parabola is obtained indicating some enhanced rate of hydration for the outer layers. As the structure was slightly pre-hydrated from the beginning, a change in hydration is hard to identify. Intuitively, one could speculate that the k-value would have been higher if the hydration experiments were performed on truly outgassed samples. However, as the k-value remains roughly at the same level regardless of the layer, it seems that H_2O does not encounter much hinder as it enters the structure.

The TCNQ-infused sample shows a maximum at the outer layers which gradually recedes as the centre is neared. The rate of hydration reduces for each layer towards the centre. From the images depicted in Figure 4.5 the same trend can be recognized, as the outer layers are readily hydrated but the crystal centre's hydration is delayed. This implies that, unlike the pristine sample, H_2O encounters some hinder at the outer layers which prevents it from diffusing towards the crystal centre.

In the right-hand graph of Figure 4.10 the maximum change in absorbance for each layer is depicted. Two parabolas are found with the maxima at the same layer. The parabola for TCNQ is sharper, indicating a larger change in absorbance of the OH-stretch vibration for that layer, which in turn means a larger concentration change of H_2O. This can be reconciled with the

interpretation of the k vs radius graph. Considering the fact that the diffusion of H_2O is hindered more at the surface for the TCNQ-infused sample than the pristine sample, one could assume that H_2O accumulates at the outer layers. The accumulation would have to visible in the total change in absorbance, which is shown in the A vs radius graph. This is in contrast to the pristine sample, which allows for less hindered diffusion, as both the k-value and A-value remain relatively unchanged per layer.

4.3 Conclusion

In the previous chapter it was concluded that an increased concentration of TCNQ was found at the crystal edge. This could have profound implications with respect to the diffusion of H_2O. Previous research points out that TCNQ positions itself across the pores of HKUST-1.[8] In Figure 1.5 one can see that TCNQ spans across the pores and binds at the Cu-paddlewheels. Considering that H_2O also prefers to bind at those locations, these two molecules could compete for the location. Furthermore, as TCNQ turns out to be situated mainly at the crystal edges, it is plausible to assume that the porous network is occluded, effectively preventing H_2O from diffusing towards the crystal centre.

This is investigated by means of *in situ* IR microscopy, where 2D single wavelength intensity maps are rendered at regular time intervals. By doing so, the distribution of H_2O could be monitored over time. The spatially resolved analysis yields a difference between the TCNQ-loaded and pristine HKUST-1, visualized in Figure 4.10. The rate of hydration seems to decrease towards the centre for the TCNQ-loaded crystal, whereas this is not the case for the pristine sample. As mentioned above, the position of TCNQ across the pores could explain this decrease in hydration rate. Due to the occluded pores, fewer H_2O is allowed to diffuse towards the centre than for the pristine sample, of which open pores are assumed. The decreased diffusion could in turn cause the accumulation of H_2O at the edges. One could conclude this from the right-hand graph in Figure 4.10 as the total absorbance value is larger for the TCNQ-loaded crystal. However, whether this is caused by the accumulation of H_2O or other factors is still debatable.

Heinke et al. reported on surface barriers in HKUST-1 preventing diffusion of cyclohexane to the inner crystal.[20] This is somewhat comparable to the case here, where a bulky molecule as cyclohexane enters the outer regions of the crystal and subsequently prevents further diffusion towards the inner crystal. As TCNQ is also mainly present at the outer regions, one could assume that TCNQ induces a similar surface barrier, preventing diffusion of H_2O.

Chapter 5

Hydrated State

In the dehydrated state elevated concentrations of TCNQ were found at the crystal edges. Furthermore, the hydration experiments alluded towards the accumulation of H_2O at the edges. Considering the sensitivity of a nitrile bond towards H_2O, the TCNQ-loaded crystal is imaged by Raman microscopy and scanning electron microscopy in their hydrated state.[58]

5.1 Confocal Raman microscopy

The same hexagonally shaped crystal, now fully hydrated, as in Chapter 3 has been imaged by means of Raman microscopy. For a decent comparison between the dehydrated and hydrated state, the results are depicted side by side.

The maps for the hexagonally shaped crystal are depicted in Figure 5.1. The differences are very subtle and decisive conclusions are difficult to make. Due to experimental variations, one can not compare the intensity of the same pixel over two experiments. Consequently, merely the relative intensity across various pixels can be compared over both experiments, as the intensity ratio between pixels of the same map is absolute. Or in other words: only changes in gradients over a single crystal provide information.

One can see that the discrete regions of enhanced intensity have become slightly more diffuse after hydration. This is especially the case for the intensity maps at 2226 cm^{-1} which represent the nitrile stretch. As mentioned beforehand, nitrile bonds are sensitive to H_2O and the intensity at 2226 cm^{-1} is expected to diminish after exposure to H_2O. It is difficult to observe anything else from these maps considering their subtle contributions. Therefore another PCA and clustering analysis is performed as all subtle contributions will be accounted for. That way a more weighted comparison is possible. Thee results are depicted in Figure 5.2.

From the PCA and clustering analysis results one can still recognize the same clusters in the hydrated state as in the dehydrated state. The blue clusters represent the background, the red clusters the crystal centre, the green clusters the crystal edges and various hotspots of condensed TCNQ as the orange cluster. In the dehydrated state, regions of elevated intensity are found at the edge indicating a local increase in TCNQ concentration. Conversely, for the hydrated state, the clusters situated at the edge (green) exhibit a reduced intensity at both 1605 cm^{-1} and 2226 cm^{-1}. This trend can be recognized in both the truncated triangular crystal and in the hexagonal crystal. This is best visualized by the insets on the right side of both figures. For both samples, the green spectrum (edge clusters) presented larger intensity than the red spectrum (centre clusters) in the dehydrated state whereas in the hydrated state this relation is inverted.

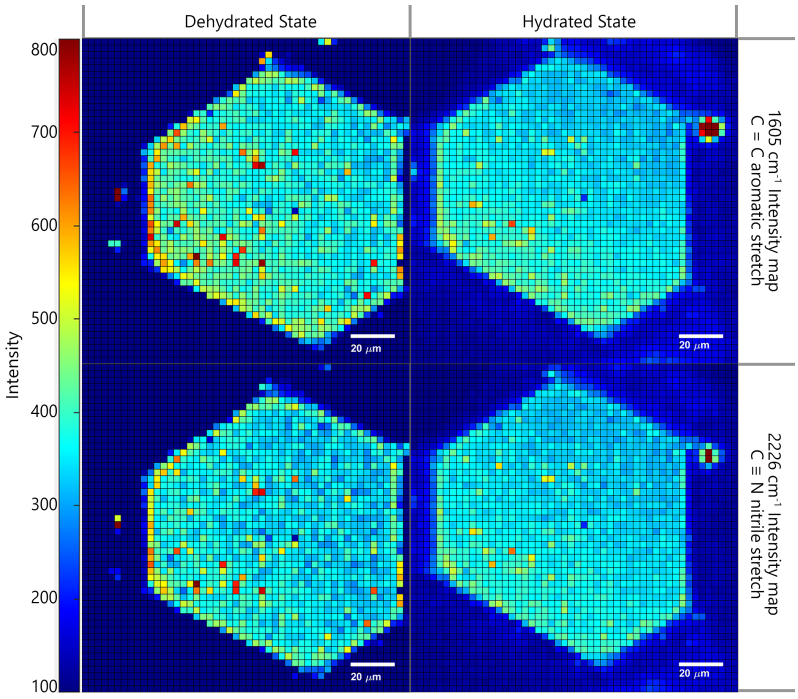

Figure 5.1: All Raman microscopy results. All maps are of the hexagonally shaped crystal. Hydration state and wavelengths are depicted in the figure.

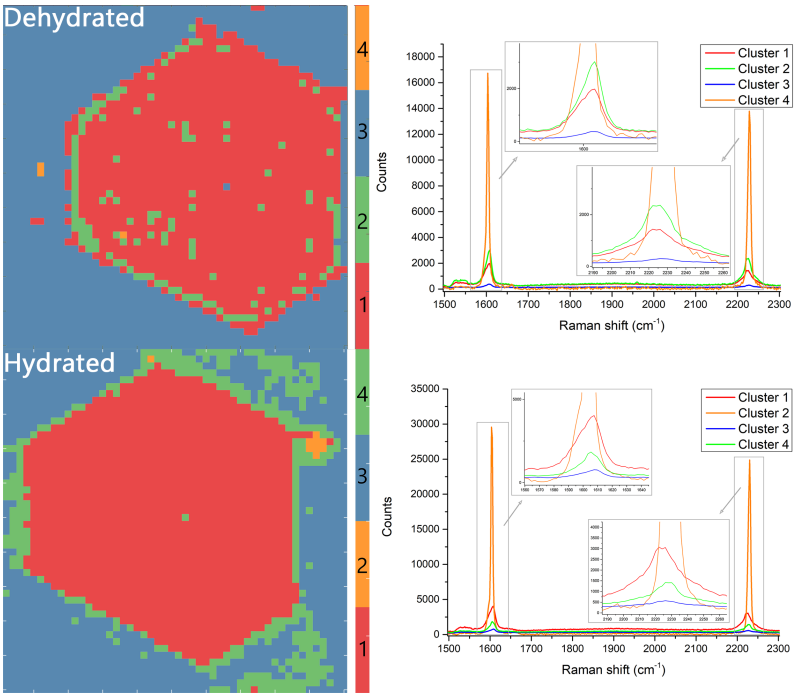

Figure 5.2: All PCA results of the Raman microscopy data. All maps are of the hexagonally shaped crystal. The hydration state is denoted in the figure.

5.2 Scanning electron microscopy

In order to support the Raman microscopy results and to elucidate any anomalies scanning electron microscopy is performed on the fully hydrated crystal.

The hexagonally shaped crystal is depicted in Figure 5.3 with the 1605 cm^{-1}Raman intensity map printed alongside it. The hotspot visible on the Raman map is most likely a contribution of the carbon tape. A black region can be seen at the same location on the SEM micrograph which does not have the same surface structure as the rest of the crystal.

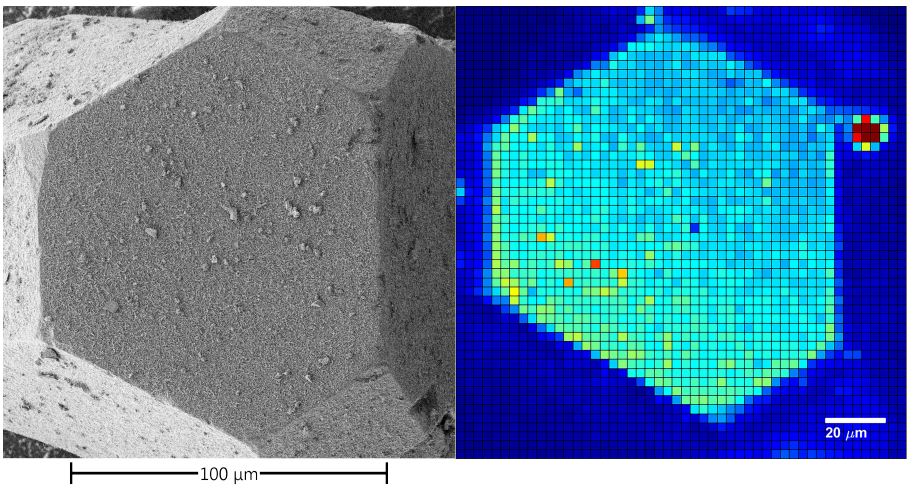

Figure 5.3: SEM micrograph of the hexagonal crystal. The Raman intensity map at 1605 cm^{-1} is depicted alongside.

Besides certain discrete regions on the crystal, the surface of both crystals was completely covered in small white filaments. It is believed that these filaments were condensed TCNQ as only the TCNQ-infused samples were covered by it. This is visualized in Figure 5.4 which are randomly chosen regions of a pristine sample and a TCNQ-infused sample. Furthermore, the imaging of

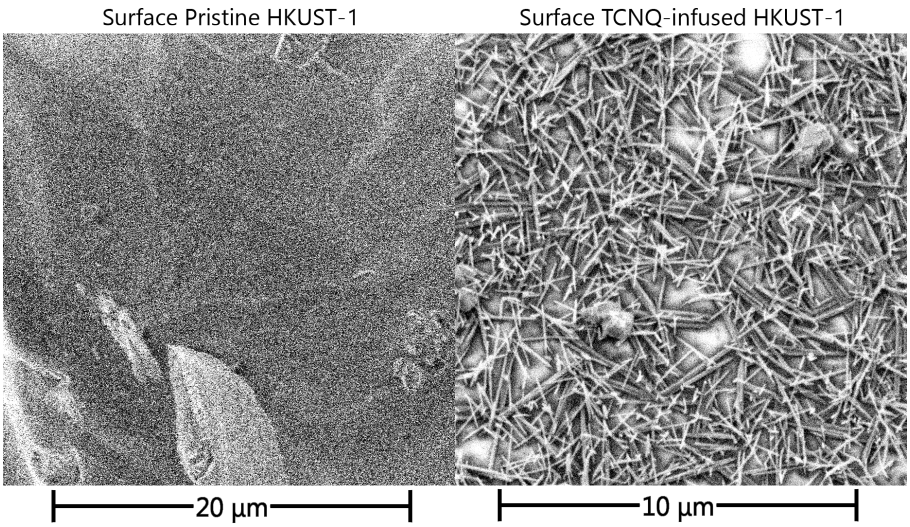

Figure 5.4: SEM micrograph both crystal's surfaces. The white filaments are believed to be condensed TCNQ.

the pristine sample was troublesome due to the sample charging under the electron probe, whereas the imaging of the TCNQ-infused samples occurred without any difficulties. As TCNQ has charge-transferring abilities, this charge build-up was also ascribed to the absence of the white filaments on the pristine sample's surface.

5.3 Conclusion

The Raman microscopy results reveal that the once discrete regions of increased TCNQ concentration have become more equally dispersed. One can see this for both single wavelength maps, as described in Chapter 3, the concentration of TCNQ is represented in both maps. The reason for the more equal dispersion is likely to be explained by the reaction of H_2O with a nitrile bond.[58] Initially, the enriched reasons of TCNQ at the edges, prevented H_2O to diffuse towards the crystal centre. This is assumed to be due to the way TCNQ is positioned in the pores. As the molecule spans across the pore, H_2O is prevented from passing through it. However, as TCNQ and H_2O react with one another, the nitrile bond could be hydrolysed, effectively opening the once occluded pore. This exposes TCNQ situated further in the crystal, prone to further hydrolysis.

Given the total hydration time (420 seconds) only TCNQ at the outer most edges is likely to react. This is in line with the PCA results depicted in Figure 5.2. From the dehydrated map it is observed that the green cluster at the crystal edge exhibits a greater intensity than the red cluster in the crystal centre. As mentioned before, this was interpreted as a TCNQ enriched edge. Yet for the hydrated map, the intensity relation between both clusters is inverted. Considering the possible degradation of TCNQ by H_2O, it is plausible that the once elevated concentration of TCNQ at the edge has diminished. Whether this lessened concentration is truly caused by hydrolysis merits further research, which will be elaborated upon in Chapter 7.

Chapter 6

Conclusions

In summary, the influence of H_2O on the TCNQ stability in electrically conductive TCNQ-incorporated HKUST-1 crystals was micro-spectroscopically investigated by comparing two crystals types: (i) bare TCNQ-free HKUST-1 and (ii) TCNQ-infused HKUST-1 crystals of similar size. TCNQ is stabilized in HKUST-1 by binding to Cu paddlewheel coordinatively unsaturated sites, which compete with H_2O under humid conditions. It is thus worthwhile to investigate the effect pf H_2O on the stability of TCNQ, since destabilization of TCNQ inside HKUST-1 could affect its function as promoter of the electric conductivity.

Ex-situ Raman micro-spectroscopy prior to humid exposure shows enhanced TCNQ intensity (C≡N, 2260 cm^{-1}) at the crystal edges, indicating preferential adsorption of TCNQ at the crystal boundaries. TCNQ is known to span across the pores of HKUST-1, which could act as a surface barrier after initial adsorption at the crystal edges. This could hinder full TCNQ prenetration to the HKUST-1 crystal core during liquid phase solvent exchange. Even though SEM imaging suggests some degree of TCNQ condensation at the HKUST-1 crystal external surface, the increased TCNQ intensity is observed tens of micrometers inside the crystal, suggesting the formation of a true crystal shell region with increased TCNQ concentration. This is further corroborated comparing the Raman C≡N intensities of real TCNQ condensates outside the crystal, which show TCNQ intensities an order of magnitude higher compared to the intensities observed inside the TCNQ-enriched crust.

After determination of the distribution of TCNQ, hydration experiments of both crystal types are performed, imaging the crystals using IR microscopy at regular intervals in between H_2O vapour pulses to monitor the distribution of H_2O. Unsurprisingly, the total concentration of H_2O increased throughout the crystals, but similar to the Raman experiments regions of increased concentration are identified at the crystal edges. For unequivocal determination of crystal heterogeneities an algorithm is devised which calculated the absorbance as a function of each crystal's radius. After fitting the calculated results with a one-phase association function improved insight into heterogeneous diffusion parameters troughout the crystals could be obtained on a qualitative level.

The experiments pointed out that the TCNQ-enriched crust did act as a barrier, effectively hindering the diffusion of H_2O. The spatially resolved analysis suggested that H_2O was not able to freely diffuse through the TCNQ-enriched crust and accumulated at the edge. As opposed to the bare TCNQ-free HKUST-1, which allowed for freer diffusion. This could be recognized by the fact that no accumulated H_2O at the crystal edge was identified and the concentration in the crystal centre increased at a greater pace than for the TCNQ-infused crystal. Considering that TCNQ will span across the crystal's pores it is plausible to assume that it will hamper the diffusion of H_2O. The accumulation of H_2O at the crystal edge for the TCNQ-infused crystal suggests that this could be the case.

Ex-situ Raman micro-spectroscopy imaging after H_2O treatment points out that the crystal edge region of initially increased TCNQ intensity disappeared and became equally distributed across the HKUST-1 crystal. Regions of increased TCNQ intensity are still present, yet the

gradients are smoother. Furthermore, the absolute crystal edge presents intensity values which are comparatively lower than the values from the crystal center. This is opposite to the initial situation – prior to H_2O treatment – where increased TCNQ intensities were observed at the HKUST-1 crystal edges. It is therefore suggested that H_2O hydrolyzes C≡N-Cu bonds, resulting in a more gradual redistribution of TCNQ across the HKUST-1 crystal. Indeed, in-situ IR microscopy shows that H_2O accumulates at the crystal edges, being the region of initially increased TCNQ, which could allow for such hydrolysis and redistribution phenomenon.

Preliminary experiments at the Fischer and Allendorf group suggest that TCNQ incorporation in the HKUST-1 structure in water-free environments does not result into significantly higher electric conductivities. However, when the synthesis is performed in humid atmospheres, electric conductivity sensibly enhances. Our results suggest that this might be caused by a more gradual distribution of TCNQ across the HKUST-1 crystal, instead of its local concentration at the crystal edge, owing to H_2O-induced hydrolysis of TCNQ-Cu bonds.

Chapter 7

Outlook

As one could have noticed, most conclusions and interpretations were presented with a great deal of nuance. This is mainly due to approximations made in order to gain scientifically insightful data. However, the downside of this approach is the compromise in generalization and statistical significance. In order to improve upon this, experimental validation and complementary experiments are worthwhile to perform. In addition, larger crystals with prolonged hydration periods could shed more light on the true nature of surface barriers. Especially considering the limited spatial resolution that IR microscopy offers, most conclusion had to be drawn based on a limited number of pixels. All these factors culminated in a qualitative evaluation rather than persuasive conclusions. However, besides a more diligent approach, there are many other factors which merit further research.

Complementary techniques such as UV-Vis microscopy would be useful, considering the colour change due to the adsorption of guest species. With the coordination chemistry occurring at the copper paddle wheels during gas adsorption, analysis of electronic states would be very interesting. Especially spatially resolved analysis would yield great additions to the IR and Raman microscopy data.

Continuing the trend of microscopy, Roeffaers et al. utilized confocal fluorescence microscopy on HKUST-1 crystals to visualize structural defects[59]. They have loaded single crystals with furfuryl alcohol as a fluorescent label in order to visualize the structure. This approach could also work for the TCNQ-infused crystals, considering TCNQ's conjugated π-systems, which would enable further analysis on the distribution of TCNQ throughout the MOF structure. Especially as this could provide a clearer signal than the conducted Raman microscopy experiments, where the true origin of the signal was a mixture of the organic linker and the TCNQ molecule.

As mentioned at the end of Chapter 6, it could be that TCNQ acts as a 'protective layer' as it seems to prevent H_2O entering the pore structure of HKUST-1. But as the nitrile bond in TCNQ is sensitive to H_2O, it is expected that the Cu-N bond would gradually hydrolyse. The molecule could subsequently dissociate from the structure, as it is bound to the copper paddle wheels at the nitrile groups. This would in turn lead to H_2O being able to freely diffuse through the MOF structure.

In order to test this hypothesis, experiments with prolonged hydration could be performed as the hydrolysis is a slow process. However, the hydrolysis can be base or acid catalysed, which merits similar bulk diffusion experiments with vaporised aqueous acids and bases. Dependent on the MOF structure's stability towards acids and bases, this could grant new insights into whether TCNQ is easily displaced from HKUST-1's pores.

Acknowledgements

After spending a year at the Inorganic Chemistry and Catalysis group, my time has come at an end. During my stay I have met a great deal of nice people, whom have all contributed to my overall project. First and foremost, I would like to thank my daily supervisor Matthias Filez. His critical approach and questions made me dig further and more diligently into my research, which has paid off. I was allowed to work autonomously, which I appreciated greatly, yet I was offer great support continuously. Furthermore, I would also like to thank Bert Weckhuysen and Pieter Bruijnincx as secondary supervisor and examiner.

For the synthesis of the TCNQ-infused HKUST-1 samples I would like to thank Christian Schneider of the Technische Univesität München. Among many others, I'd like to thank some people who helped me either with experiments or with valuable discussions. Miguel Rivera Torrente, who virtually acted as another supervisor. Thanks for all the help regarding XRD and all MOF-related discussions. Also for being the link with Christian Schneider and actually enabling me to work on this topic. For the help with the SEM measurements I would like to thank Jochem Wijten. Thanks to Thomas Hartman and Suzanne Verkleij for helping me to start up with Raman microscopy and IR microscopy. Furthermore, I would like to thank all the members of the Vibrational Spectroscopy team. I've obtained some great insights from the meeting and also some necessary corrections.

And last but not least, the Master students with whom I had all kinds of work-(un)related discussions which made my stay here memorable. Thanks for a great experience.

Ewout van der Feltz

Bibliography

[1] B. Liu, H. Shioyama, H. Jiang, X. Zhang, and Q. Xu. Metal-organic framework (MOF) as a template for syntheses of nanoporous carbons as electrode materials for supercapacitor. *Carbon*, 48(2):456–463, 2010.

[2] L. E. Kreno, K. Leong, O. K. Farha, M. Allendorf, R. P. Van Duyne, and J. T. Hupp. Metal-organic framework materials as chemical sensors. *Chemical Reviews*, 112(2):1105–1125, 2012.

[3] P. Horcajada, C. Serre, M. Vallet-Regí, M. Sebban, F. Taulelle, and G. Férey. Metal-organic frameworks as efficient materials for drug delivery. *Angewandte Chemie*, 45(36):5974–5978, 2006.

[4] J. Lee, O. K. Farha, J. Roberts, K. A. Scheidt, S. T. Nguyen, and J. T. Hupp. Metalorganic framework materials as catalysts. *Chemical Society Reviews*, 38(5):1450, 2009.

[5] H. Li, M. Eddaoudi, M. O'Keeffe, and O. M. Yaghi. Design and synthesis of an exceptionally stable and highly porous metal-organic framework. *Nature*, 402:276–279, 1999.

[6] M. Ranocchiari and J. A. van Bokhoven. Catalysis by metalorganic frameworks: fundamentals and opportunities. *Physical Chemistry Chemical Physics*, 13(14):6388, 2011.

[7] J. Li, R. J. Kuppler, and H. Zhou. Selective gas adsorption and separation in metalorganic frameworks. *Chemical Society Reviews*, 38(5):1477, 2009.

[8] A. A. Talin, A. Centrone, A. C. Ford, M.E. Foster, V. Stavila, P. Haney, R. A. Kinney, V. Szalai, F. El Gabaly, H. P. Yoon, F. Léonard, and M. D. Allendorf. Tunable Electrical Conductivity in Metal-Organic Framework Thin-Film Devices. *Science*, 343(6166):66–69, 2014.

[9] Schoedel Laboratory. "Design of Porous Frameworks from First Principles" http://research3.fit.edu/schoedel/research.php (accessed February 13, 2018).

[10] S. S. Y. Chui, S. M. F. Lo, J. P. H. Charmant, A. G. Orpen, and I. D. Williams. A Chemically Functionalizable Nanoporous Material [Cu3(TMA)2(H2O)3]n. *Science*, 283(5405):1148–1150, 1999.

[11] M. K. Bhunia, J. T. Hughes, J. C. Fettinger, and A. Navrotsky. Thermochemistry of paddle wheel MOFs: Cu-HKUST-1 and Zn-HKUST-1. *Langmuir*, 29:8140–8145, 2013.

[12] N. Al-Janabi, P. Hill, L. Torrente-Murciano, A. Garforth, P. Gorgojo, F. Siperstein, and X. Fan. Mapping the Cu-BTC metal-organic framework (HKUST-1) stability envelope in the presence of water vapour for CO2 adsorption from flue gases. *Chemical Engineering Journal*, 281:669–677, 2015.

[13] A. O. Yazaydin, A.I. Benin, S. A. Faheem, P. Jakubczak, J. J. Low, R. R. Willis, and R.Q. Snurr. Enhanced CO2 Adsorption in Metal-Organic Frameworks via Occupation of Open-Metal Sites by Coordinated Water Molecules. *Chemistry of Materials*, 21(13):1425–1430, 2009.

[14] W. W. Lestari, R. E. Nugraha, I. D. Winarni, M. Adreane, and F. Rahmawati. Optimization on electrochemical synthesis of HKUST-1 as candidate catalytic material for Green diesel production. *AIP Conference Proceedings*, 1725(May), 2016.

[15] C. Graham, D. A. Imrie, and R. E. Raab. Measurement of the electric quadrupole moments of CO2, CO, N2, Cl2 and BF3. *Molecular Physics*, 93(1):49–56, 1998.

[16] S. D. Worrall, M. A. Bissett, W. Hirunpinyopas, M. P. Attfield, and R. A. W. Dryfe. Facile fabrication of metal-organic framework HKUST-1-based rewritable data storage devices. *Journal of Matererials Chemistry C*, 4(37):8687–8695, 2016.

[17] L. H. Wee, M. R. Lohe, N. Janssens, S. Kaskel, and J. A. Martens. Fine tuning of the metalorganic framework Cu3(BTC)2 HKUST-1 crystal size in the 100 nm to 5 micron range. *Journal of Materials Chemistry*, 22(27):13742, 2012.

[18] M. Todaro, G. Buscarino, L. Sciortino, A. Alessi, F. Messina, M. Taddei, M. Ranocchiari, M. Cannas, and F. M. Gelardi. Decomposition Process of Carboxylate MOF HKUST-1 Unveiled at the Atomic Scale Level. *Journal of Physical Chemistry C*, 120(23):12879–12889, 2016.

[19] G. Majano, O. Martin, M. Hammes, S. Smeets, C. Baerlocher, and J. Pérez-ramírez. Solvent-Mediated Reconstruction of the Metal Organic Framework HKUST-1 (Cu3(BTC)2). *Advanced Functional Materials*, 1:3855–3865, 2014.

[20] L. Heinke, Z. Gu, and C. Wöll. The surface barrier phenomenon at the loading of metal-organic frameworks. *Nature communications*, 5(May):4562, 2014.

[21] I. E. Craven, M. R. Hesling, D. R. Laver, P. B. Lukins, G. L. D. Ritchie, and J. Vrbancich. Polarizability anisotropy, magnetic anisotropy, and quadrupole moment of cyclohexane. *Journal of Physical Chemistry*, 93(2):627–631, 1989.

[22] P. G. Gucciardi, S. Trusso, C. Vasi, S. Patane, and M. Allegrini. Nano-Raman imaging of CuTCNQ clusters in TCNQ thin films by scanning near-field optical microscopy. *Physical Chemistry Chemical Physics*, 4(12):2754–2753, 2002.

[23] S. Mosleh, M. R. Rahimi, M. Ghaedi, K. Dashtian, and S. Hajati. Photocatalytic degradation of binary mixture of toxic dyes by HKUST-1 MOF and HKUST-1 SBA-15 in a rotating packed bed reactor under blue LED illumination: central composite design optimization. *RSC Advances*, 6(21):17204–17214, 2016.

[24] C. H. Hendon and A. Walsh. Chemical principles underpinning the performance of the metal organic framework HKUST-1. *Chememical Science*, 6(7):3674–3683, 2015.

[25] C. Prestipino, L. Regli, J. G. Vitillo, F. Bonino, A. Damin, C. Lamberti, A. Zecchina, P. L. Solari, K. O. Kongshaug, and S. Bordiga. Local structure of framework Cu(II) in HKUST-1 metallorganic framework: Spectroscopic characterization upon activation and interaction with adsorbates. *Chemistry of Materials*, 18(5):1337–1346, 2006.

[26] P. Küsgens, M. Rose, I. Senkovska, H. Fröde, A. Henschel, S. Siegle, and S. Kaskel. Characterization of metal-organic frameworks by water adsorption. *Microporous and Mesoporous Materials*, 120(3):325–330, 2009.

[27] J. Liu, A. M. B. Furtado, P. Jakubczak, R. R. Willis, and M. D. Levan. Stability Effects on CO 2 Adsorption for the DOBDC Series of Metal À Organic Frameworks. *Langmuir*, 27:11451–11456, 2011.

[28] L. Hamon, E. Jolima, and G. D. Pirngruber. CO 2 and CH 4 Separation by Adsorption Using Cu-BTC Metal - Organic Framework. *Industrial and Engineering Chemistry Research*, 49:7497–7503, 2010.

[29] J. Liu, Y. Wang, P. Jakubczak, R. R. Willis, and M. D. Levan. CO2/H2O Adsorption Equilibrium and Rates on Metal - Organic Frameworks: HKUST-1 and Ni/DOBDC. *Langmuir*, 26(19):14301–14307, 2010.

[30] C. Huygens and S. P. Thompson. *Treatise on Light*. Macmillan And Company., Limited, 1912.

[31] W. H. Bragg and W. L. Bragg. The Reflection of X-rays by Crystals. *Proceedings of the Royal Society London A.*, 88:428–438, 1913.

[32] A. T. Young. Rayleigh scattering. *Applied Optics*, 20(4):533–535, 1981.

[33] S. A. Speakman. Basics of X-Ray Powder Diffraction - Training to Become an Independent User of the X-Ray SEF at the Center for Materials Science and Engineering at MIT [PowerPoint slides].

[34] A. J. Den Dekker and A. Van Den Bos. Resolution : a survey. *Journal of the Optical Society of America A*, 14(3):547–557, 1997.

[35] M. A. van Huis and H. Friedrich. Nanoparticles: Workhorses of Nanoscience. In Celso De Mello Donegá, editor, *Nanoparticles: Workhorses of Nanoscience*, chapter 7 Electron, pages 191–222. 2014.

[36] F. Krumeick. *Properties of electrons, their interactions with matter and applications in electron microscopy*. Thesis, Zurich, 2011.

[37] A. Zumbusch, G. R. Holtom, and X. S. Xie. Three-Dimensional Vibrational Imaging by Coherent Anti-Stokes Raman Scattering. *Physical Review Letters*, 82(20):1–4, 1999.

[38] M. J. Baker, S. R. Hussain, L. Lovergne, V. Untereiner, C. Hughes, R. A. Lukaszewski, G. Thiefin, and G. D. Sockaalingum. Developing and understanding biofluid vibrational spectroscopy: a critical review. *Chemical Society Reviews*, 45:1803–1818, 2016.

[39] Psychology & Neuroscience. (2018-01-11). Retrieved from https://psychology.stackexchange.com /questions/13829/voltage-sensitive-dyes-technique-2-photons-microscopy-vs-confocal-microscopy.

[40] T. Dieing, O. Hollricher, and J. Toporski. *Confocal raman microscopy*. Springer, 2011.

[41] Stephen W. Paddock, Thomas J. Fellers, and Michael W. Davidson. Paddock, Stephen W. Fellers, Thomas J. Davidson, Michael W. (2018-01-11). Confocal Microscopy. Retrieved from https://nikon.magnet.fsu.edu/articles/confocal/confocalintrobasics.html.

[42] P. R. Griffiths and E. V. Miseo. *Infrared and Raman spectroscopic imaging*. Number September. Wiley-VCH, Weinheim, Germany, 2014.

[43] R. Salzer and H. W. Siesler. *Infrared and Raman Spectroscopic Imaging*. Wiley-VCH, Weinheim, Germany, 2009.

[44] T. M. Tovar, J. Zhao, W. T. Nunn, H. F. Barton, G. W. Peterson, G. N. Parsons, and M. D. LeVan. Diffusion of CO2 in Large Crystals of Cu-BTC MOF. *Journal of the American Chemical Society*, 138(36):11449–11452, 2016.

[45] I. T. Joliffe. *Principal Component Analysis and Factor Analysis*, volume 42. 2002.

[46] R. Bro and A. K. Smilde. Principal component analysis. *Anal. Methods*, 6(9):2812–2831, 2014.

[47] R. R. Meglen. Examining large databases: a chemometric approach using principal component analysis. *Marine Chemistry*, 39(1-3):217–237, 1992.

[48] J. E. Jackson. *A User's Guide To Principal Compenents*, volume 26. 2003.

[49] Z. Ristanović, J. P. Hofmann, M. I. Richard, T. Jiang, G. A. Chahine, T. U. Schülli, F. Meirer, and B. M. Weckhuysen. X-ray Excited Optical Fluorescence and Diffraction Imaging of Reactivity and Crystallinity in a Zeolite Crystal: Crystallography and Molecular Spectroscopy in One. *Angewandte Chemie*, 55(26):7496–7500, 2016.

[50] H. Zha, X. He, C. Ding, and H. Simon. Spectral Relaxation for K-means Clustering. *MIT Press*, pages 1057—-1064, 2001.

[51] C. Ding and X. He. K-means clustering via principal component analysis. *Proceedings of the twenty-first international conference on Machine learning*, (2000):29, 2004.

[52] J. A. Hartigan and M. A. Wong. A K-Means Clustering Algorithm. *Journal of the Royal Statistical Society. Series C (Applied Statistics)*, 28(1):100–108, 1979.

[53] J Macqueen. *Some methods for classification and analysis of multivariate observations*, volume 1. 1967.

[54] M. R. Gupta. Theory and Use of the EM Algorithm. *Foundations and Trends in Signal Processing*, 4(3):223–296, 2010.

[55] C. E. Rasmussen. The infinite Gaussian mixture model. *Advances in Neural Information Processing Systems*, (1):554–560, 2000.

[56] Z. Zivkovic. Improved adaptive Gaussian mixture model for background subtraction. *Proceedings of the 17th International Conference on Pattern Recognition*, (May):28–31 Vol.2, 2004.

[57] J. Ethiraj, F. Bonino, C. Lamberti, and S. Bordiga. H2S interaction with HKUST-1 and ZIF-8 MOFs: A multitechnique study. *Microporous and Mesoporous Materials*, 207:90–94, 2015.

[58] Vadim Yu Kukushkin and Armando J.L. Pombeiro. Metal-mediated and metal-catalyzed hydrolysis of nitriles. *Inorganica Chimica Acta*, 358(1):1–21, 2005.

[59] R. Ameloot, F. Vermoortele, J. Hofkens, F. C. De Schryver, D. E. De Vos, and M. B. J. Roeffaers. Three-dimensional visualization of defects formed during the synthesis of metal-organic frameworks: A fluorescence microscopy study. *Angewandte Chemie*, 52(1):401–405, 2013.

Appendix A

A.1 PCA justification

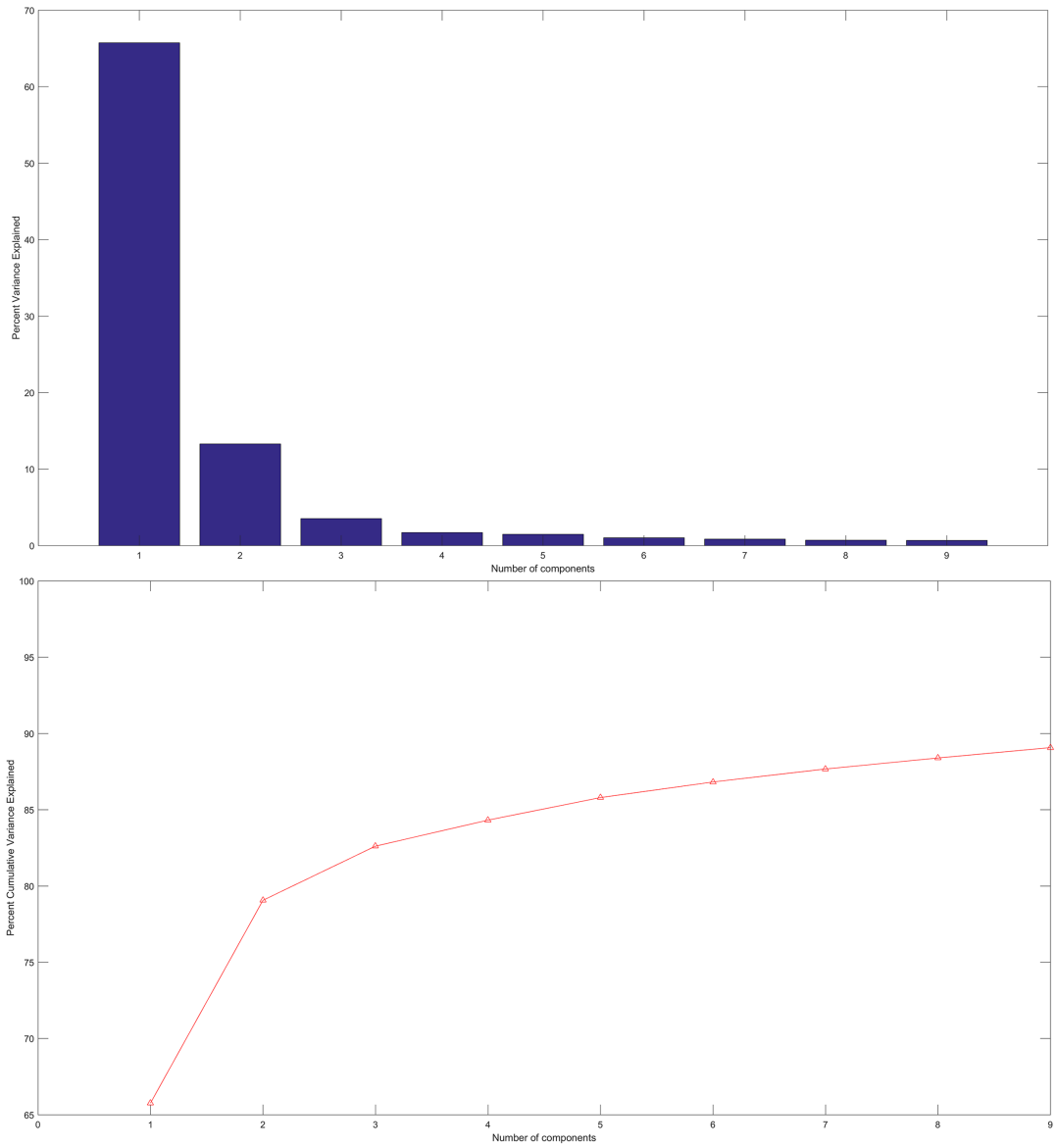

Figure A.1: Cumulative variance explained of each principle component.

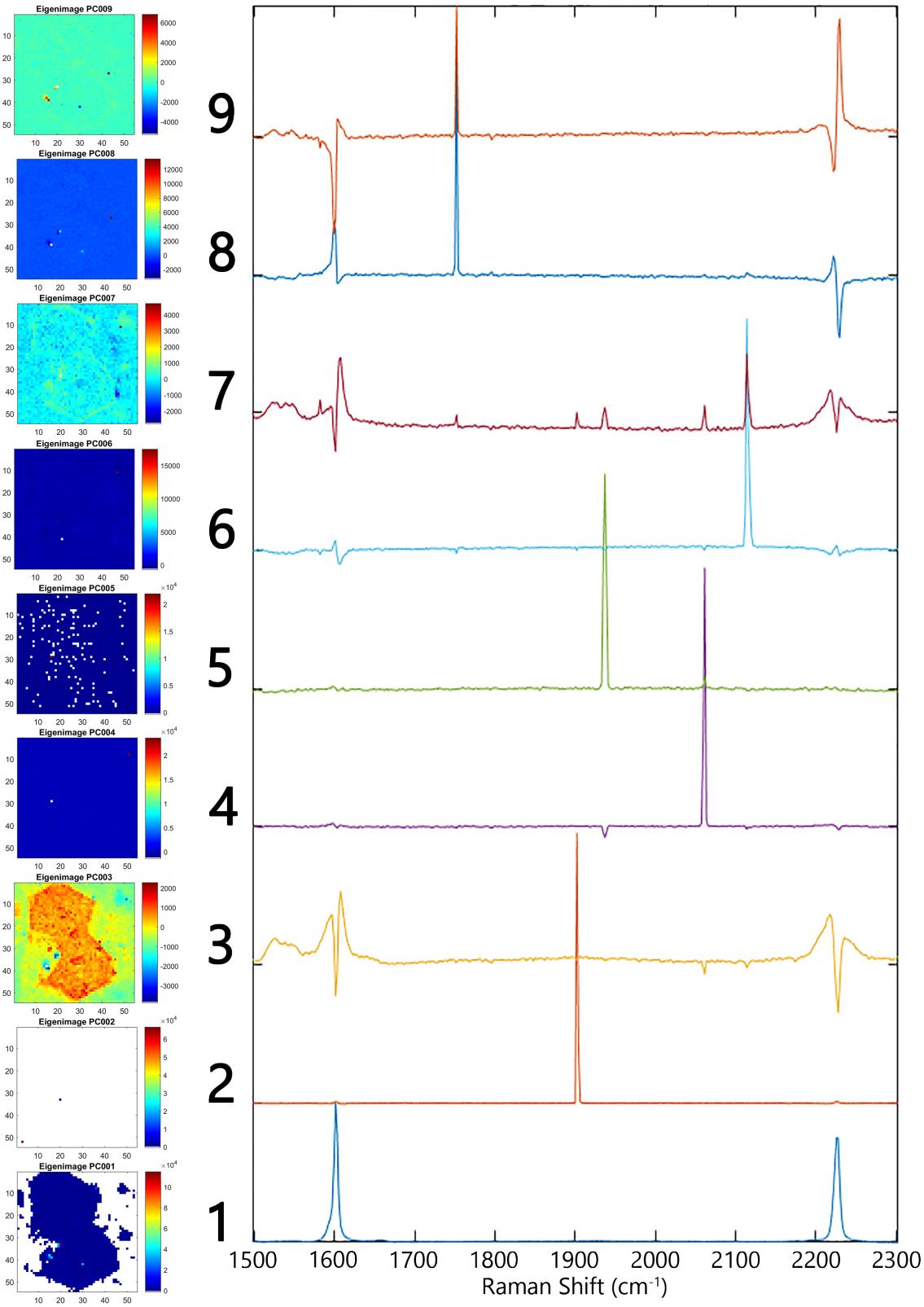

Figure A.2: All eigenimages and associated eigenspectra of the PCA results described in Figure 3.2.

A.2 Relevant Matlab scripts

Raman data processing

```
%Raman Mapping Script
%% Supply data in desired format for pcolor function:
[fname,pname]=uigetfile('C:\Users\Ewout\Dropbox\Personal Storage\Documents\Scheikunde\
    Master\Masters Research\Data\Processed Data\Raman\180119_MapsDepthSeriesAndSlices\
    Maps\*.txt','Please select the data file.');
wbh = waitbar(0,'Converting data ... please wait');
D = dlmread(fullfile(pname,fname),'\t');

X = unique(D(:,1));
Y = unique(D(:,2));
nX = size(X,1);
nY = size(Y,1);
nSpectPts = (size(D,1)/nX)/nY;
%M=D;
% convert to matrix: spectral point x Y x X:
% for special case unfinished data set; only works for this specific case:
%nSpectPts = 391;
%DD = zeros(39*103*391,4);
%nX = 39; nY = 103;
%DD(1:size(D,1),:)=D;
%D = DD;
M  = reshape(D(:,4),[nSpectPts,nY,nX]);
% if it was recorded in snake mode:
wbh1 = waitbar(1,'Correcting snake mode ... please wait');
   for ii=1:nSpectPts
        M(ii,:,2:2:end) = flipud(squeeze(M(ii,:,2:2:end)));
        waitbar(ii/nSpectPts,wbh1);
   end
close(wbh1);
M = permute(M, [2 3 1]);
SignalMatrix = M(:,:,352);
%SignalMatrix = flip(SignalMatrix);
%SignalMatrix = flip(SignalMatrix,2);
emptycolumn = zeros(size(SignalMatrix,1),1);
emptyrow = zeros(1,size(SignalMatrix,2)+1);
SignalMatrix = [SignalMatrix emptycolumn];
SignalMatrix = [SignalMatrix;emptyrow];
close(wbh)

%% Generate pseudocolorplot
    f = figure;
        pcolor(SignalMatrix);
    view(90,90)
    %Define title and space marker
    unitstring = '\mum';
    titlestring = sprintf('HKUST-1 TCNQ Infused 2226 cm^{-1} \n %i %s x %i %s Raman
        Intensity Map',(3*size(M,2)),unitstring,(3*size(M,1)),unitstring);
    title(titlestring,'FontSize',22)
    xlabel('X dimension (\mum)','FontSize',20)
    ylabel('Y dimension (\mum)','FontSize',20)
    set(gca,'xtick',[])
    set(gca,'ytick',[])
    rectangle('Position', [51.5 46 .5 6.666], 'FaceColor','w','EdgeColor','white');
    text(53,46,'20 \mum','Color','w','FontSize',18,'FontWeight','bold');
    %Add colorbar with corresponding label
    colorbar
    colormap(jet(1000))
    h = colorbar;
    ylabel(h, 'Counts', 'FontSize', 15)
    %Defines desired upper and lower signal limit
    caxis([0 1400])
    set(gcf,'InnerPosition',[-1835 42 1082 954])

    %% File coding
    filename = sprintf('%s%s.png',pname,titlestring(1:33));
    frm = getframe(f);
    imwrite(frm.cdata, filename)
    close(f)
```

FTIR data processing

Mask definition

```
    %% Input Parameters
InputFolder = uigetdir('MATLABrootFolder','Select Directory');


%% Metadata and references
addpath(InputFolder)
ParentFolder = strcat(InputFolder,'\');
InputFolder_FSM = strcat(ParentFolder,'*.fsm');
FsmData = dir(InputFolder_FSM);

%% Main body code
wb = waitbar(0,'Converting .fsm to .tif files...');
for i = 1:size(FsmData,1)
    FSM = fsmload(FsmData(i).name);              %Generates MxNxP array.
                                                 %M columns = X-axis pixels
                                                 %N rows = Y-axis pixels
                                                 %P pages = Wavenumbers 1 = 4000 cm-1, end
                                                    = 690 cm-1
                                                 %Value = Transmission in %
    %Convert to Absorbance
    FSM_Abs = 2 - log10(FSM);

    % rescale to 16bit, i.e. [0 65535]:
    % 5 bits for red colors, 6 bits for green, 5 bits for blue
    FSMmin = min(min(min(FSM_Abs)));
    FSM_Abs = FSM_Abs-FSMmin;
    FSMmax = max(max(max(FSM_Abs)));
    FSM_Abs = uint16((FSM_Abs./FSMmax).*65535);

    %Define Seperate Wavenumber .txt file
    xStart = 4000;
    xEnd = 1000;
    SpecRes = round((xEnd - xStart)/1000);
    N = 1000;
    Wavenumbers = xStart + (0:N-1)*SpecRes;
        Wavenumbers = Wavenumbers.';

    %Define .TIFs folder per .fsm
    Folder = sprintf('%s_TIFs',FsmData(i).name);
    mkdir(InputFolder,Folder);
    %Print Wavenumber file
    Wvn = sprintf('%s%s/Wavenumbers.txt',ParentFolder,Folder);
    dlmwrite(Wvn,Wavenumbers);
    %Define text format .tif files
    Wvn_prefix = FsmData(i).name(1:end-5);
    Wvn_prefix = strrep(Wvn_prefix,'%','_');
    %Print .tif file for each wavenumber
    for ii=1:1000
        Wvn = sprintf('%s%s/%05i_%s.tif',ParentFolder,Folder,ii,Wvn_prefix);
        imwrite(rot90(squeeze(FSM_Abs(:,:,ii))),Wvn);
    end
    waitbar(i/size(FsmData,1))
end
close(wb)
```

Radial absorbance

The first 36 lines are merely lines for robustness of the code. Lines 39-66 define the mask for the samples. The bulk code is represented by lines 70-127. Initially, an m x n blank template array (`aveAbsorbanceEdge`) is defined containing a cell for each shell's absorbance value along dimension m (rows) and each .fsm file along dimension n (columns). Subsequently, a for-loop will execute code for each .fsm file and print the output along successive columns of the template array. Abovementioned code contains another for-loop for each 'shell' of the crystal. A 2D single wavelength intensity plot at 3400 cm^{-1} (`OH_Band`)is generated (`intensityArray`) and the mask (`thresholdBlock`) is overlayed. The edge pixels are indexed, their absorbance values assessed and the average value is printed along the rows of the template array. As the output is printed, the indexed pixels (`linearInd`) are void of their content (converted to `NaN`), effectively discarding the outer edge and exposing the next shell. In the next iteration, the new edges are indexed, the absorbance is assesed, printed and their contents converted to `NaN`. Each iteration reduces the size of the shell until all pixel's contents are converted to NaN. At this point, the first for-loop iterates to the following .fsm file and absorbance values for each shell are assessed. Finally, the template (`aveAbsorbanceEdge`) is filled with all absorbance values and printed to a .txt file.

The indexing of edge pixels occurs over two directions. Each single wavelength intensity plot is effectively a 32 x 32 matrix with all background pixel values set as `NaN`. MATLAB's `find` function, provides the matrix coordinates of either the first or last entry in a row or column vector. By indexing the first and last value of each row and column, all edges of the crystal are accounted for. The `unique` function eliminates any duplicates as vertex pixels are indexed twice by the `find` function. All values of `intensityArray` are assessed by the indices and averaged.

```
inputFolder = uigetdir('MATLABrootFolder','Select Directory');
pixelSize = 6.25;
unitString = '\mum';

%% Metadata and references
addpath(inputFolder)
parentFolder = strcat(inputFolder,'\');
    Folder = 'Images';
    if isdir(strcat(parentFolder,Folder)) == 0
            mkdir(inputFolder,Folder);
    end

fsmData = dir(strcat(inputFolder,'\*.fsm'));
%Calculate array indices for wavenumbers of interest
refFsm = fsmload(fsmData(1).name);
    Linker_Band1 = round(size(refFsm,3)/(3310/(4000-1388)));          %Value
        corresponding to 1388 cm-1
    Linker_Band2 = round(size(refFsm,3)/(3310/(4000-1456)));          %Value
        corresponding to 1456 cm-1
    Linker_Band3 = round(size(refFsm,3)/(3310/(4000-1660)));          %Value
        corresponding to 1660 cm-1
    TCNQ_Band1   = round(size(refFsm,3)/(3310/(4000-2000)));          %Value
        corresponding to 2000 cm-1
    TCNQ_Band2   = round(size(refFsm,3)/(3310/(4000-2229)));          %Value
        corresponding to 2229 cm-1
    BG_Band      = round(size(refFsm,3)/(3310/(4000-2500)));          %Value
        corresponding to 2500 cm-1
    Hexane_Band  = round(size(refFsm,3)/(3310/(4000-2969)));          %Value
        corresponding to 2969 cm-1
    OH_Band      = round(size(refFsm,3)/(3310/(4000-3400)));          %Value
        corresponding to 3400 cm-1

%Generate 4D array of all .fsm files
fsmBlock = zeros(size(refFsm,1),size(refFsm,2),size(refFsm,3),size(fsmData,1));
    %Dimension 1 = Y-pixels,     Dimension 2 = X-Pixels,
    %Dimension 3 = Wavenumbers, Dimension 4 = #.fsm file (time dim)
wb1 = waitbar(0,'Importing .fsm files');
for i = 1:size(fsmData,1)
    fsmBlock(:,:,:,i) = fsmload(fsmData(i).name);
    waitbar(i/size(fsmData,1),wb1);
end
%Convert to absorbance
fsmBlock = 2 - log10(fsmBlock);
close(wb1)

%% Define mask threshold
```

```
firstFsm = fsmBlock(:,:,:,1);
    %First TwinSamples Pristine
     firstFsm_875 = firstFsm(:,:,875);
     threshold = firstFsm_875 >= 1.35; %2D Mask

thresholdBlock = false(size(refFsm,1),size(refFsm,2),size(refFsm,3)); %3D Mask
for ii = 1:size(fsmBlock,3)
    thresholdBlock(:,:,ii) = threshold;
end


%% Bulk body code
wb2 = waitbar(0,'Calculating absorbance');
aveAbsorbanceEdge = NaN(15,size(fsmData,1));


for iii = 1:size(fsmData,1)
    %Apply mask
    fsm = NaN(1+size(refFsm,1),1+size(refFsm,2),size(refFsm,3));
    fsmRaw = fsmBlock(:,:,:,iii);
    fsmRaw(thresholdBlock) = NaN;
    fsm(1:end-1,1:end-1,:) = fsmRaw;

        %Generate intensity plot
        intensityArray = fsm(:,:,OH_Band);

        for r = 1:size(aveAbsorbanceEdge,1)
            f = figure;
            pcolor(intensityArray)
            %Generate position of edge pixels as linear indices
            linearInd = ones(size(intensityArray,1),4);
            edgeAbsorbances = zeros(1,4);
            for row = 1:size(intensityArray,1)
                if numel(intensityArray(~isnan(intensityArray(row,:)))) == 0
                    linearInd(row,1:2) = 1;
                else
                linearInd(row,1) = sub2ind(size(intensityArray),row,find(~isnan(
                    intensityArray(row,:)),1,'first')); %Left border
                linearInd(row,2) = sub2ind(size(intensityArray),row,find(~isnan(
                    intensityArray(row,:)),1,'last'));  %Right border
                end
            end
            for col = 1:size(intensityArray,2)
                if numel(intensityArray(~isnan(intensityArray(:,col)))) == 0
                    linearInd(col,3:4) = 1;
                else
                linearInd(col,3) = sub2ind(size(intensityArray),find(~isnan(
                    intensityArray(:,col)),1,'first'),col); %Bottom border
                linearInd(col,4) = sub2ind(size(intensityArray),find(~isnan(
                    intensityArray(:,col)),1,'last'),col);  %Top Border
                end
            end

            %Generate absorbance values of edge pixels
            linearInd = unique(linearInd);
            edgeAbsorbances = sum(intensityArray(linearInd),'omitnan');

            nPixels = size(linearInd,1);

            aveAbsorbanceEdge(r,iii) = sum(edgeAbsorbances)/nPixels;

            intensityArray(linearInd) = NaN;

            close(f)
        end
    waitbar(iii/size(fsmData,1),wb2);
end

filename = sprintf('%s%s/Absorbance over Radius.txt',parentFolder,Folder);
dlmwrite(filename,aveAbsorbanceEdge);

close(wb2)
```